PHYSICAL REVIEW D **93,** 042002 (2016)

Observing gravitational waves from core-collapse supernovae in the advanced detector era

S. E. Gossan,[1,2] P. Sutton,[4] A. Stuver,[5,6] M. Zanolin,[3] K. Gill,[3] and C. D. Ott[2]

[1]*LIGO—California Institute of Technology, Pasadena, California 91125, USA*
[2]*TAPIR, MC 350-17, California Institute of Technology, Pasadena, California 91125, USA*
[3]*Embry Riddle Aeronautical University, 3700 Willow Creek Road, Prescott, Arizona 86301, USA*
[4]*Cardiff University, Cardiff, CF24 3AA, United Kingdom*
[5]*LIGO Livingston Observatory, Livingston, Louisiana 70754, USA*
[6]*Louisiana State University, Baton Rouge, Louisiana 70803, USA*

(Received 9 November 2015; published 5 February 2016)

The next galactic core-collapse supernova (CCSN) has already exploded, and its electromagnetic (EM) waves, neutrinos, and gravitational waves (GWs) may arrive at any moment. We present an extensive study on the potential sensitivity of prospective detection scenarios for GWs from CCSNe within 5 Mpc, using realistic noise at the predicted sensitivity of the Advanced LIGO and Advanced Virgo detectors for 2015, 2017, and 2019. We quantify the detectability of GWs from CCSNe within the Milky Way and Large Magellanic Cloud, for which there will be an observed neutrino burst. We also consider extreme GW emission scenarios for more distant CCSNe with an associated EM signature. We find that a three-detector network at design sensitivity will be able to detect neutrino-driven CCSN explosions out to ∼5.5 kpc, while rapidly rotating core collapse will be detectable out to the Large Magellanic Cloud at 50 kpc. Of the phenomenological models for extreme GW emission scenarios considered in this study, such as long-lived bar-mode instabilities and disk fragmentation instabilities, all models considered will be detectable out to M31 at 0.77 Mpc, while the most extreme models will be detectable out to M82 at 3.52 Mpc and beyond.

DOI: 10.1103/PhysRevD.93.042002

I. INTRODUCTION

Core-collapse supernovae (CCSNe) are driven by the release of gravitational energy in the core collapse of massive stars in the zero-age-main-sequence mass range $8M_\odot \lesssim M \lesssim 130M_\odot$. The available energy reservoir of ∼300 Bethe (B, $1\mathrm{B} = 10^{51}$ erg) is set by the difference in gravitational binding energy of the precollapse core ($R \sim 1000$–2000 km, $M \sim 1.4M_\odot$) and the collapsed remnant ($R \sim 10$–15 km). Much of this energy is initially stored as heat in the protoneutron star and most of it (∼99%) is released in the form of neutrinos, ∼1% goes into the kinetic energy of the explosion, ∼0.01% is emitted across the electromagnetic (EM) spectrum, and an uncertain, though likely smaller, fraction will be emitted in gravitational waves (GWs) [1,2].

Distant CCSNe are discovered on a daily basis by astronomers. Neutrinos from CCSNe have been observed once, from the most recent nearby CCSN, SN 1987A [3,4], which occured in the Large Magellanic Cloud (LMC), roughly 52 kpc from Earth [5]. GWs[1] are—at lowest and likely dominant order—emitted by quadrupole mass-energy dynamics. In the general theory of relativity, GWs have two polarizations, denoted plus (+) and cross (×). Passing GWs will lead to displacements of test masses that are directly proportional to the amplitudes of the waves and, unlike EM emission, not their intensity. GWs have not yet been directly detected.

GWs, much like neutrinos, are emitted from the innermost region (the core) of the CCSN and thus convey information on the dynamics in the supernova core to the observer. They potentially carry information not only on the general degree of asymmetry in the dynamics of the CCSN, but also more directly on the explosion mechanism [1,10,11], on the structural and compositional evolution of the protoneutron star [12–15], the rotation rate of the collapsed core [16–19], and the nuclear equation of state [17,20,21].

A spherically symmetric CCSN will not emit GWs. However, EM observations suggest that many, if not most, CCSN explosions exhibit asymmetric features (e.g., [22–26]). This is also suggested by results of multidimensional CCSN simulations (e.g., [27–35] and references therein). Spherical symmetry should be robustly broken by stellar rotation, convection in the protoneutron star and in the region behind the CCSN shock, and by the standing accretion shock instability (SASI [36]). The magnitude and time variation of deviations from spherical symmetry, and thus the strength of the emitted GW signal, are uncertain and likely vary from event to event [1,13]. State-of-the-art models, building upon an extensive body of theoretical work on the GW signature of CCSNe, predict GW strains—relative displacements of test masses in a detector on Earth—h of order 10^{-23}–10^{-20} for a core

[1]For detailed reviews of GW theory and observation, we refer the reader to Refs. [6–9].

collapse event at 10 kpc, signal durations of 1 ms − few s, frequencies of ∼1 − few 1000 Hz, and total emitted energies $E_{\rm GW}$ of 10^{41}–10^{47} erg (corresponding to 10^{-12}–$10^{-7} M_{\odot} c^2$) [1,13,14,17,27,29,37–40]. More extreme phenomenological models, such as long-lasting rotational instabilities of the proto-neutron star and accretion disk fragmentation instabilities, associated with hypernovae and collapsars, suggest much larger strains and more energetic emission, with $E_{\rm GW}$ perhaps up to 10^{52} erg ($\sim 0.01 M_{\odot} c^2$) [41–44].

Attempts to detect GWs from astrophysical sources were spearheaded by Weber in the 1960s [45]. Weber's detectors and other experiments until the early 2000s relied primarily on narrow-band ($\lesssim$10 s of Hz) resonant bar or sphere detectors (e.g., [46]). Of these, NAUTILUS [47], AURIGA [48], and Schenberg [49] are still active. The era of broadband GW detectors began with the kilometer-scale first-generation laser interferometer experiments. The two 4-km LIGO observatories [50] are in Hanford, Washington, and Livingston, Louisiana, hereafter referred to as H1 and L1, respectively. A second 2-km detector was located in Hanford, referred to as H2, but was decommissioned at the end of the initial LIGO observing runs. The 3-km Virgo detector [51] is located in Cascina, Italy. Other GW interferometers are the 300-m detector TAMA300 [52] in Mitaka, Japan, and the 600-m detector GEO600 [53] in Hanover, Germany. The second generation of ground-based laser interferometric GW detectors, roughly 10 times more sensitive than the first generation, are under construction. The two Advanced LIGO detectors [54] began operation in late 2015 at approximately one-third of their final design sensitivity, jointly with GEO-HF [55]. Advanced Virgo [56] will commence operations in 2016, followed by KAGRA [57] later in the decade. LIGO India [58] is under consideration, and may begin operations c. 2022.

Typically, searches for GW transients must scan the entire GW detector data set for signals incident from any direction on the sky (e.g., [59,60] and references therein) unless an external "trigger" is available. The observation of an EM or neutrino counterpart can provide timing and/or sky position information to localize the prospective GW signal (e.g., [61–63] and references therein). The sensitivity of GW searches utilizing external triggers can be more sensitive by up to a factor of ∼2, as constraints on time and sky position help reduce the background noise present in interferometer data (e.g., [61,64]). In both cases, networks of two or more detectors are typically required to exclude instrumental and local environmental noise transients that could be misindentified as GW signals. This is particularly important in the case where there is no reliable model for the GW signal, such as for CCSNe.

Arnaud *et al.* [65] were the first to make quantitative estimates on the detection of GWs from CCSNe. They studied the detectability of GW signals from axisymmetric rotating core collapse [66], by means of three different filtering techniques. The authors showed that, in the context of stationary, Gaussian noise with zero-mean, the signals should be detectable throughout the galaxy with initial Virgo [51].

Ando *et al.* [67], using single-detector data taken with the TAMA300 interferometer, were the first to carry out an untriggered all-sky blind search specifically for GWs from rotating core collapse. These authors employed a model-independent approach which searches for time-frequency regions with excess power compared to the noise background (called an "excess power method" (e.g., [68–71]). They employed rotating core-collapse waveforms from Dimmelmeier *et al.* [72] to place upper limits on detectability and rate of core collapse events in the Milky Way. Unfortunately, these upper limits were not astrophysically interesting due to the high false alarm rate of their search, caused by their single-detector analysis and the limited sensitivity of their instrument.

Hayama *et al.* [73] studied the detectability of GWs from multidimensional CCSN simulations from [38,74–76]. Using the coherent network analysis network pipeline `RIDGE` [77], signals in simulated Gaussian noise for a four-detector network containing the two Advanced LIGO detectors, Advanced Virgo, and KAGRA are considered. The authors find that GWs from the neutrino-driven explosions considered are detectable out to ∼(2–6) kpc, while GWs from rapidly rotating core-collapse and nonaxisymmetric instabilities are detectable out to between ∼(11–200) kpc.

In this article, we describe a method for the detection of GWs from CCSNe in nonstationary, non-Gaussian data recolored to the predicted sensitivity of the second-generation interferometers. Since GW emission from CCSNe may be very weak (but can vary by orders of magnitudes in strain, frequency content, and duration), we follow a triggered approach and employ `X-Pipeline` [78], a coherent analysis pipeline designed specifically to detect generic GW transients associated with astrophysical events such as gamma-ray bursts and supernovae using data from networks of interferometers. We consider

(1) CCSNe within ∼50 kpc with sky position and timing localization information provided by neutrinos (e.g., [79–81]). At close source distances, we hope to detect GWs from CCSNe in current scenarios predicted by state-of-the-art multidimensional numerical simulations.
(2) Distant CCSNe with sky position and timing localization information provided by EM observations. At distances greater than ∼(50–100) kpc, we do not expect to detect GWs from the conservative emission scenarios predicted by multidimensional CCSN simulations. Instead, we consider more extreme, phenomenological emission models. These may be unlikely to occur, but have not yet been constrained observationally.

We consider GW emission from "garden-variety" CCSNe (e.g. convection, SASI, and rotating core collapse and bounce) with waveform predictions from multidimensional CCSN simulations, in addition to extreme postcollapse GW emission mechanisms. In addition, we consider for both scenarios sine-Gaussian GW bursts as an *ad hoc* model for GW signals of central frequency f_0 and quality factor Q, which are frequently used to assess the sensitivity of searches for generic GW bursts of unknown morphological shape [59,60].

This paper is organized as follows. In Sec. II, we discuss the challenges associated with observing GWs from CCSNe. We outline our strategies to overcome these challenges and introduce the observational scenarios considered in this study in Sec. III. We review the waveforms from multidimensional hydrodynamic simulations and phenomenological waveform models used in this study in Sec. IV. In Sec. V, we give details of our analysis approach and lay out how we establish upper limits for detectability. We present the results of our analysis and provide quantitative estimates for the distances out to which GWs may be observed for each of the considered waveform models and detector sensitivity in Sec. VI. We summarize and conclude in Sec. VII.

II. CHALLENGES

GW astronomers looking for short-duration GW transients emitted from CCSNe face multiple challenges.

A. The rate of observable events is low

If GW emission in standard, "garden-variety" CCSNe occurs at the strains and frequencies predicted by current models, simple estimates of signal-to-noise ratios (SNRs) suggest that even second-generation detectors may be limited to detecting core-collapse events in the Milky Way and the Small and Large Magellanic Clouds [1,12,14,29]. The expected rate of CCSNe in the Milky Way is $\sim(0.6-10.5)\times10^{-2}$ CCSNe yr^{-1}, (e.g., [82–87]), and it is $\sim(1.9-4.0)\times10^{-3}$ CCSNe yr^{-1} in the combined Magellanic Clouds [82,84,88].

Similar SNR estimates for extreme GW emission models for CCSNe suggest that they may be observable throughout the Local Group and beyond ($D\lesssim20$ Mpc). Within the Local Group ($D\lesssim3$ Mpc), the CCSN rate is $\sim9\times10^{-2}$ CCSNe yr^{-1}, with major contributions from Andromeda (M31), Triangulum (M33), and the dwarf irregular galaxy IC 10, IC 1613, and NGC 6822 [82,84,89,90]. Outside of the Local Group, the CCSN rate increases to ~0.15 CCSNe yr^{-1} within $D\sim5$ Mpc, including IC 342, the M81 group, M83, and NGC 253 as significant contributors to the CCSN rate [91–96]. Within $D=10$ Mpc, the CCSN rate is ~0.47 CCSNe yr^{-1}, while it increases to ~2.1 CCSNe yr^{-1} within $D=20$ Mpc [91,94–96].

B. The duty cycle of the detectors is not 100%

The fraction of time interferometers are operating and taking science-quality data is limited by several factors including commissioning work (to improve sensitivity and stability) and interference due to excessive environmental noise.

For example, consider LIGO's fifth science run (S5), the data from which we use for the studies in this paper. S5 lasted almost two years between November 15, 2005 and November 2, 2007, and the H1, H2, and L1 detectors had duty cycles of 75%, 76%, and 65%, respectively. The duty cycle for double coincidence (two or more detectors taking data simultaneously) was 60%, and the triple coincidence duty cycle was 54% [97,98]. The risk of completely missing a CCSN GW signal is mitigated by having a larger network of detectors. In addition, resonant bar and sphere detectors do provide limited backup [47–49].

C. The noise background in the GW data is non-Gaussian and nonstationary

Noise in interferometers arises from a combination of instrumental, environmental, and anthropomorphic noise sources that are extremely difficult to characterize precisely [50,99–101]. Instrumental "glitches" can lead to large excursions over the time-averaged noise and may mimic the expected time-frequency content of an astrophysical signal [50,102]. Mitigation strategies against such noise artifacts include

(1) Coincident observation with multiple, geographically separated detectors
(2) Data quality monitoring and the recording of instrumental and environmental vetos derived from auxiliary data channels such as seismometers, magnetonometers, etc.
(3) Glitch-detection strategies based on Bayesian inference (e.g., [103,104]) or machine learning (e.g., [104,105])
(4) Using external triggers from EM or neutrino observations to inform the temporal "on-source window" in which we expect to find GW signals and consequently reduce the time period searched.

D. The gravitational wave signal to be expected from a core-collapse event is uncertain

The time-frequency characteristics of the GW signal from a core-collapse event is strongly dependent on the dominant emission process and the complex structure, angular momentum distribution, and thermodynamics of the progenitor star. In the presence of stochastic emission processes (e.g., fluid instabilities such as convection and SASI), it is impossible to robustly predict the GW signal. As a result, the optimal method for signal extraction, matched (Wiener) filtering [106], cannot be used, as a robust, theoretical prediction of the amplitude and phase of

the GW signal is required. Matched filtering is typically used in searches for GWs from compact binary coalescence, for which robust signal models exist.

The "excess-power" approach [69–71] is an alternative to matched filtering for signals of uncertain morphology. Searching for statistically significant excesses of power in detector data in the time-frequency plane, prior information on the sky position, time of arrival, and polarization of the targeted GW source can be exploited to reduce the noise background and, consequently, the detection false alarm rate. It can be shown that, in the absence of any knowledge of the signal other than its duration and frequency bandwidth, the excess-power method is Neyman-Pearson optimal in the context of Gaussian noise [69].

III. OBSERVATIONAL SCENARIOS

Core-collapse events are the canonical example of multi-messenger astrophysical sources and, as such, are particularly suited to externally triggered GW searches. In this section, we describe four potential observational scenarios for CCSNe in the local Universe.

A. Location of SNe

We consider CCSNe in four galaxies that contribute significantly to the CCSN rate in the Local Group and Virgo cluster.

The Milky Way, a barred spiral galaxy, is the galaxy that houses our solar system. For the purposes of this study, we consider a CCSN in the direction of the Galactic center, at right ascension (RA) $17^{\mathrm{h}}47^{\mathrm{m}}21.5^{\mathrm{s}}$ and declination (Dec) $-5°32'9.6''$ [107], located ∼9 kpc from Earth. This is motivated by the work of Adams *et al.* ([87]), in which the probability distribution for the distance of galactic CCSN from Earth is shown to peak around ∼9 kpc, and the CCSN location distribution is assumed to trace the disk of the galaxy. The galactic CCSN rate is estimated at $(0.6-10.5)\times 10^{-2}$ CCSNe yr^{-1} [87], and the youngest known galactic CCSN remnant, Cassiopeia A, is believed to be ∼330 yrs old [108].

The Large Magellanic Cloud (LMC) is home to the most active star-formation region in the Local Group, the Tarantula Nebula [109]. Located at RA $5^{\mathrm{h}}23^{\mathrm{m}}34.5^{\mathrm{s}}$ and Dec $-69°45'22''$ [110], the LMC is an irregular galaxy located ∼50 kpc from Earth [111,112], and is estimated to have a CCSN rate of $(1.5-3.1)\times 10^{-3}$ CCSNe yr^{-1} [82,84]. The last CCSN observed in the LMC was SN1987A, a type II-pec SN first detected on February 23, 1987, by Kamiokande II via its neutrino burst [3].

The M31 galaxy, also referred to as Andromeda, is the most luminous galaxy in the Local Group. Located at RA $0^{\mathrm{h}}42^{\mathrm{m}}44.4^{\mathrm{s}}$ and Dec $41°16'8.6''$ [113], M31 is a spiral galaxy located ∼0.77 Mpc from Earth [114], and is estimated to have a CCSN rate of $\sim 2.1\times 10^{-3}$ CCSNe yr^{-1} [82,84]. No CCSNe have yet been observed from M31.

The M82 galaxy, five times brighter than the Milky Way, exhibits starburst behavior incited by gravitational interaction with M81, a neighboring galaxy [115]. Located at RA $9^{\mathrm{h}}55^{\mathrm{m}}52.7^{\mathrm{s}}$ and Dec $69°40'46''$ [116], M82 is an irregular starburst galaxy at a distance ∼3.52 Mpc from Earth [117]. Its CCSN rate is estimated to be $\sim(2.1-20)\times 10^{-2}$ CCSNe yr^{-1} [118,119]. The most recent CCSN in M82 was SN2008iz, a Type II SN first observed on May 3, 2008 [120].

We summarize the relevant information on the aforementioned galaxies in Table I.

B. Analysis times

The SuperNova Early Warning System (SNEWS) [121] Collaboration aims to provide a rapid alert for a nearby CCSN to the astronomical community, as triggered by neutrino observations. CCSNe within ∼100 kpc will have an associated neutrino detection. The Large Volume Detector (LVD), a kiloton-scale liquid scintillator experiment [122], and Super-Kamiokande (Super-K), a water-imaging Cerenkov-detector [123], will be able to detect neutrinos from a CCSN with full detection probability (100%) out to 30 kpc and 100 kpc, respectively [123,124]. BOREXINO (a 300-ton liquid scintillator experiment [125]) is able to detect all galactic CCSNe [126], while IceCube (a gigaton-scale long string particle detector made of Antarctic ice [127]) can detect a CCSN in the Large Magellanic Cloud at 6σ confidence. For CCSNe within ∼0.66 kpc, KamLAND (a kiloton-scale liquid scintillator detector [128]) will be able to detect neutrinos from pre-SN stars at 3σ confidence [129].

Pagliaroli *et al.* [80] were the first to make quantitative statements on the use of neutrino detection from CCSNe as external triggers for an associated GW search, in the context of an analytical approximation for the anti-electron neutrino luminosity, $L_{\bar{\nu}_e}$, as a function of time. More realistic models for L_ν (see, e.g. [130,131]) suggest that over ∼95% of the total energy in neutrinos is emitted

TABLE I. Summary of the location, distance, and CCSN rate of the four host galaxies considered.

Galaxy name	Right ascension (degrees)	Declination (degree)	Distance [Mpc]	CCSN rate [$\times 10^{-2}$ yr^{-1}]	References
Milky Way	266.42	−29.01	0.01	0.6–10.5	[87]
LMC	80.89	−69.76	0.05	0.1–0.3	[82,84,110,112]
M31	10.69	41.27	0.77	0.2	[82,84,113,114]
M82	148.97	69.68	3.52	2.1–20	[116–119]

TABLE II. Summary of the observational counterpart used to derive the on-source window, in addition to the associated on-source window, for type Ibc and type II SNe in the four considered host galaxies.

Galaxy name	Observational counterpart	On-source window for type Ibc [s]	On-source window for type II [s]
Milky Way	Neutrino, EM	$[-10, +50]$	$[-10, +50]$
LMC	Neutrino, EM	$[-10, +50]$	$[-10, +50]$
M31	EM	$[-60, +3600]$	$[-180000, +3600]$
M82	EM	$[-60, +86400]$	$[-180000, +86400]$

within ~10 s of core bounce. Given the neutrino observation time, t_0, we consider a 60 s on-source window, aligned $[-10, 50]$ s about t_0. We note that a more detailed neutrino light curve will allow the time of core bounce to be localized to ~few ms [132]. This would permit the use of a much shorter on-source window, resulting in a lower background rate and higher detection sensitivity.

For more distant CCSNe, the neutrino burst from core collapse will likely not be detected, but an EM counterpart will be observed. The on-source window derived from the EM observation time is dependent on progenitor star characteristics (i.e. progenitor star radius, shock velocity), as well as the observation cadence. The first EM signature of a CCSN comes at the time of shock breakout, $t_{\rm SB}$, when the shock breaks through the stellar envelope.

Type Ib and type Ic SNe, hereafter referred to jointly as type Ibc SNe, have very compact progenitors ($R_* \sim$ few$(1-10)R_\odot$) and have been stripped of their stellar envelopes through either intense stellar winds (i.e. Wolf-Rayet stars) or mass transfer to a binary companion [133,134]. Li ([135]) studied the properties of shock breakout for a variety of type Ibc SN progenitor models in the context of semianalytic density profiles and found shock breakout times in the range $t_{\rm SB} \in [1, 35]$s. As a conservative estimate, we choose $t_{\rm SB,min} = 60$ s.

For type II SNe, however, the progenitors are supergiant stars. Type II-pec SNe, such as SN1987A, have blue supergiant progenitors, with typical stellar radii of $\sim 25R_\odot$. More typically, the progenitors are red supergiant stars, with typical stellar radii of $\sim(100\text{–}1000)R_\odot$ [133,134]. Hydrodynamic simulations of type II-P SN progenitors from Bersten *et al.* [136] and Morozova *et al.* [137] show typical breakout times of $t_{\rm SB} \sim$ few10 h. As a conservative estimate, we consider the unstripped type II-P progenitor from Morozova *et al.* [137] and use $t_{\rm SB,max} = 50$ h.

In addition to theoretical predictions of the time to shock breakout, the cadence of observations of the CCSN host galaxy must be considered when deriving the on-source window. For actively observed galaxies, we expect to have no greater than ~24 h latency between pre- and post-CCSN observations. We consider two observational scenarios in which the time scale between pre- and post-CCSN images are $t_{\rm obs} \sim 1$ h and 24 h, for sources in M31 and M82, respectively. We construct the on-source window assuming that shock breakout occurs immediately after the last pre-SN image. Given the time of the last pre-SN observation, the EM trigger time t_0, we consider an on-source window of length $t_{\rm SB} + t_{\rm obs}$, aligned $[-t_{\rm SB}, t_{\rm obs}]$ about t_0.

We summarize the on-source windows used for all observational scenarios considered in Table II.

The strain detected by a GW interferometer, $h(t)$, is given by

$$h(t) = F_+(\theta, \Phi, \psi)h_+(t) + F_\times(\theta, \Phi, \psi)h_\times(t), \quad (1)$$

where $F_{+,\times}(\theta, \Phi, \psi)$ are the antenna response functions of the detector to the two GW polarizations, $h_{+,\times}(t)$. For a source located at sky position (θ, Φ) in detector-centered coordinates, and characterized by polarization angle ψ, $F_{+,\times}$ are given by

$$\begin{aligned} F_+ &= \frac{1}{2}(1+\cos^2\theta)\cos 2\phi \cos 2\psi - \cos\theta \sin 2\phi \sin 2\psi, \\ F_\times &= \frac{1}{2}(1+\cos^2\theta)\cos 2\phi \sin 2\psi - \cos\theta \sin 2\phi \cos 2\psi. \end{aligned} \quad (2)$$

The antenna response of the detectors is periodic with an associated time scale of one sidereal day, due to the rotation of the Earth. As a consequence, the sensitivity of GW searches using on-source windows much shorter than this time scale will be strongly dependent on the antenna response of the detectors to the source location at the relevant GPS time. In Fig. 1, we show the sum-squared antenna response for each detector over one sidereal day, for sources located at the Galactic center, LMC, and M31. As the sensitivity of the detector network is a function of time, we wish to choose a central trigger time t_0 for which the antenna sensitivity is representative of the average over time. To represent the time-averaged sensitivity of the detector network, we choose GPS trigger times of $t_0 = 871645255$, $t_0 = 871784200$, and $t_0 = 871623913$ for the Galactic, LMC, and M31 sources, respectively. For CCSNe in M82, relying on low-cadence EM triggers, the shortest considered on-source window is longer than one sidereal day and, as such, the entire range of antenna responses is encompassed during the on-source window. We choose GPS trigger time $t_0 = 871639563$ for the M82 source, such that the 74 h on-source window is covered by the 100 h stretch of S5 data recolored for this study.

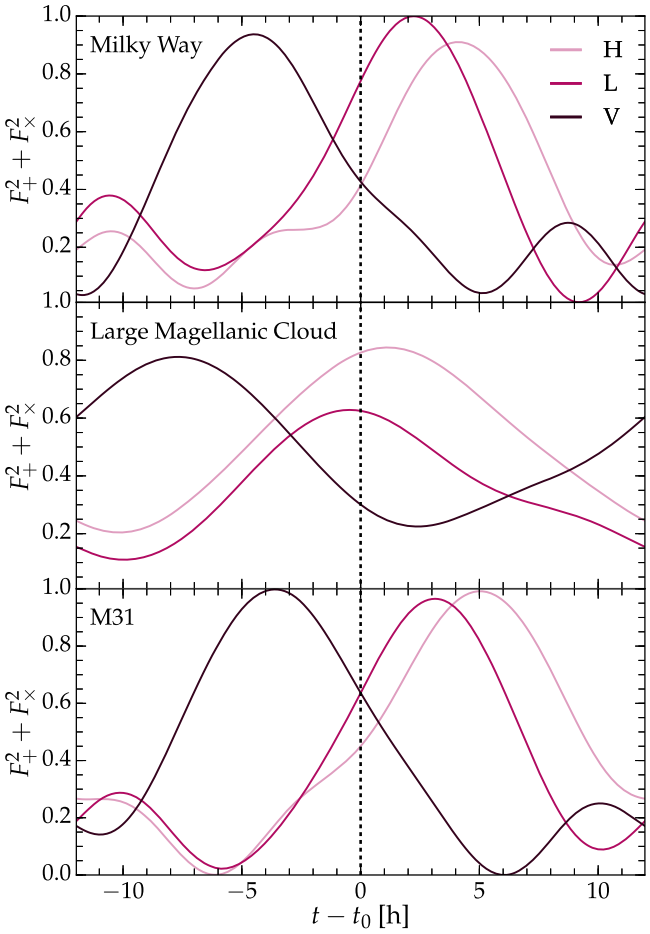

FIG. 1. The sum-squared antenna response, $F^2 = F_+^2 + F_\times^2$, over one mean sidereal day for the two Advanced LIGO detectors (H,L), and the Advanced Virgo detector, V, for sources located toward the Galactic center (top), LMC (middle), and M31 (bottom). For each galaxy, we indicate the chosen GPS trigger time t_0 with a dashed black line.

C. Detector networks

As mentioned previously, the GW detector noise will be non-Gaussian and nonstationary. To this end, we use real GW data from the fifth LIGO science run (S5) and the first Virgo science run (VSR1), recolored to the target noise amplitude spectra densities (ASDs)[2] for the considered observational scenarios. See Sec. V B for technical details on the recoloring procedure used.

We consider a subset of the observing scenarios outlined in Aasi *et al.* [138] to explore how the sensitivity of the Advanced detectors to CCSNe will evolve between 2015 and 2019. For all these cases, we characterize the detector sensitivity by the single-detector binary neutron star (BNS) range, $d_{\rm R}$. The BNS range is the standard figure of merit for detector performance, and is defined as the sky location- and orientation-averaged distance at which a $(1.4, 1.4)M_\odot$ BNS system can be detected with an SNR, $\rho \geq 8$. The 2015 scenario assumes a two-detector network comprised of the two Advanced LIGO detectors (H,L) operating with BNS range $d_{\rm R;HL} = 54$ Mpc and is hereafter referred to as the `HL 2015` scenario. The 2017 scenario assumes a three-detector network comprised of the two Advanced LIGO detectors (H,L) operating with BNS range $d_{\rm R;HL} = 108$ Mpc, and the Advanced Virgo detector operating with BNS range of $d_{\rm R;V} = 36$ Mpc, and is hereafter referred to as the `HLV 2017` scenario. In 2019, we consider a three-detector network, HLV, with the two Advanced LIGO detectors operating with BNS range $d_{\rm R;HL} = 199$ Mpc, and the Advanced Virgo detector operating with BNS range $d_{\rm R;V} = 154$ Mpc, referred to as the `HLV 2019` observational scenario [56,138]. Figure 2 shows the one-sided ASDs $\sqrt{S_h(f)}$ of Advanced LIGO and Advanced Virgo as used to recolor the data for each observational scenario considered.

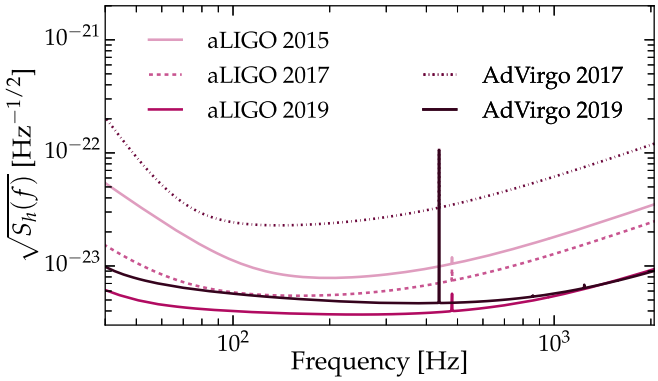

FIG. 2. The predicted amplitude spectral densities (ASDs), $\sqrt{S_h(f)}$ of the Advanced LIGO and Advanced Virgo detector noise for the considered 2015, 2017, and 2019 detector networks [56,138].

IV. GRAVITATIONAL WAVES FROM CORE-COLLAPSE SUPERNOVAE: CONSIDERED EMISSION MODELS

A broad range of multidimensional processes may emit GWs during core collapse and the subsequent postbounce CCSN evolution. These include, but are not necessarily limited to, turbulent convection driven by negative entropy or lepton gradients and the SASI (e.g., [12–14,21,37]), rapidly rotating collapse and bounce (e.g., [17,39,75]), postbounce nonaxisymmetric rotational instabilities (e.g., [38,44,139,140]), rotating collapse to a black hole (e.g., [40]), asymmetric neutrino emission and outflows [12–14], and, potentially, rather extreme fragmentation-type instabilities occuring in accretion torii around nascent neutron stars or black holes [43]. A more extensive discussion of GW emission from CCSNe can be found in recent reviews on the subject in Refs. [1,2,141]. Most of these emission

[2]The one-sided amplitude spectral density is the square root of the one-sided power spectral density, $S_h(f)$.

TABLE III. Key characteristics of "numerical" waveforms from multidimensional CCSN simulations. $E_{\rm GW}$ is the energy emitted in GWs, $\langle h_{\rm rss}\rangle$ is the angle-averaged root-sum-square strain [Eq. (11)], and $f_{\rm peak}$ is the frequency at which the spectral GW energy $\mathrm{d}E_{\rm GW}/\mathrm{d}f$ peaks.

Waveform type	Ref.	Waveform name	$\langle h_{\rm rss}\rangle$ [10^{-22} at 10 kpc]	$f_{\rm peak}$ [Hz]	$E_{\rm GW}$ [$M_\odot c^2$]
2D neutrino-driven convection and SASI	[14]	yak	1.89	888	9.08×10^{-9}
3D neutrino-driven convection and SASI	[37]	müller1	1.66	150	3.74×10^{-11}
3D neutrino-driven convection and SASI	[37]	müller2	3.85	176	4.37×10^{-11}
3D neutrino-driven convection and SASI	[37]	müller3	1.09	204	3.25×10^{-11}
3D neutrino-driven convection and SASI	[29]	ott	0.24	1019	7.34×10^{-10}
2D rotating core collapse	[17]	dim1	1.05	774	7.69×10^{-9}
2D rotating core collapse	[17]	dim2	1.80	753	2.79×10^{-8}
2D rotating core collapse	[17]	dim3	2.69	237	1.38×10^{-9}
3D rotating core collapse	[143]	sch1	5.14	465	2.25×10^{-7}
3D rotating core collapse	[143]	sch2	5.80	700	4.02×10^{-7}

mechanisms source GWs in the most sensitive frequency band of ground-based laser interferometers (~50–1000 Hz). Exceptions (and not considered in this study) are black hole formation ($f_{\rm peak}\sim$ few kHz), asymmetric neutrino emission, and asymmetric outflows ($f_{\rm peak}\lesssim 10$ Hz).

For the purpose of this study, we consider a subset of the above GW emission mechanisms and draw example waveforms from two-dimensional (2D) and three-dimensional (3D) CCSN simulations (we refer to these waveforms as numerical waveforms in the following). In addition, we construct analytical phenomenological waveforms that permit us to constrain extreme emission scenarios. We consider GW emission in the quadrupole approximation, which has been shown to be accurate to within numerical error and physical uncertainties for CCSNe [142]. In Tables III and IV, we summarize key properties of the selected numerical and phenomenological waveforms, respectively, including the total energy emitted in GWs, $E_{\rm GW}$, the angle-averaged root-sum-squared GW strain, $\langle h_{\rm rss}\rangle$, and the peak frequency of GW emission, $f_{\rm peak}$. We define $f_{\rm peak}$ as the frequency at which the spectral GW energy density, $\mathrm{d}E_{\rm GW}/\mathrm{d}f$, peaks.

We compute $E_{\rm GW}$ as in [6] from the spectral GW energy density, $\mathrm{d}E_{\rm GW}/\mathrm{d}f$, as

$$E_{\rm GW}=\int_0^\infty \mathrm{d}f\,\frac{\mathrm{d}E_{\rm GW}}{\mathrm{d}f}, \tag{3}$$

where

$$\frac{\mathrm{d}E_{\rm GW}}{\mathrm{d}f}=\frac{2}{5}\frac{G}{c^5}(2\pi f)^2|\tilde{I}_{ij}|^2, \tag{4}$$

and

$$\tilde{\ddot{I}}_{ij}(f)=\int_{-\infty}^{\infty}\mathrm{d}t\ddot{I}_{ij}(t)e^{-2\pi i f t} \tag{5}$$

is the Fourier transform of $\ddot{I}_{ij}(t)$, the second time derivative of the mass-quadrupole tensor in the transverse-traceless gauge.

To construct the strain for different internal source orientations, we present the projection of GW modes, $H_{lm}(t)$, onto the -2 spin-weighted spherical harmonic basis, ${}^{-2}Y_{lm}(\iota,\phi)$ [145]. Using this, we may write

TABLE IV. Key characteristics of the considered waveforms from phenomenological models. $E_{\rm GW}$ is the energy emitted in GWs, $\langle h_{\rm rss}\rangle$ is the angle-averaged root-sum-square strain [Eq. (11)], and $f_{\rm peak}$ is the frequency at which the spectral GW energy density $\mathrm{d}E_{\rm GW}/\mathrm{d}f$ peaks.

Waveform type	Ref.	Waveform name	$\langle h_{\rm rss}\rangle$ [10^{-20} at 10 kpc]	$f_{\rm peak}$ [Hz]	$E_{\rm GW}$ [$M_\odot c^2$]
Long-lasting bar mode	[144]	longbar1	1.48	800	2.98×10^{-4}
Long-lasting bar mode	[144]	longbar2	4.68	800	2.98×10^{-3}
Long-lasting bar mode	[144]	longbar3	5.92	1600	1.90×10^{-2}
Long-lasting bar mode	[144]	longbar4	7.40	800	7.46×10^{-3}
Long-lasting bar mode	[144]	longbar5	23.41	800	7.45×10^{-2}
Long-lasting bar mode	[144]	longbar6	14.78	1600	1.18×10^{-1}
Torus fragmentation instability	[43]	piro1	2.55	2035	6.77×10^{-4}
Torus fragmentation instability	[43]	piro2	9.94	1987	1.03×10^{-2}
Torus fragmentation instability	[43]	piro3	7.21	2033	4.99×10^{-3}
Torus fragmentation instability	[43]	piro4	28.08	2041	7.45×10^{-2}

$$h_+ - ih_\times = \frac{1}{D}\sum_{l=2}^{\infty}\sum_{m=-l}^{l} H_{lm}(t)\,{}^{-2}Y_{lm}(\iota,\phi), \tag{6}$$

where (ι,ϕ) are the internal source angles describing orientation.

It has been shown that for CCSN systems, the quadrupole approximation method of extracting GWs is sufficiently accurate [142]. As such, we consider only the $l=2$ mode and can write the mode expansion as

$$\begin{aligned} H^{\rm quad}_{20} &= \sqrt{\frac{32\pi}{15}}\frac{G}{c^4}\left(\ddot{I}_{zz} - \frac{1}{2}(\ddot{I}_{xx}+\ddot{I}_{yy})\right),\\ H^{\rm quad}_{2\pm1} &= \sqrt{\frac{16\pi}{5}}\frac{G}{c^4}(\mp\ddot{I}_{xz} + i\ddot{I}_{yz}),\\ H^{\rm quad}_{2\pm2} &= \sqrt{\frac{4\pi}{5}}\frac{G}{c^4}(\ddot{I}_{xx} - \ddot{I}_{yy} \mp 2i\ddot{I}_{xy}), \end{aligned} \tag{7}$$

and

$$\begin{aligned} {}^{-2}Y_{20} &= \sqrt{\frac{15}{32\pi}}\sin^2\iota,\\ {}^{-2}Y_{2\pm1} &= \sqrt{\frac{5}{16\pi}}\sin\iota(1\pm\cos\iota)e^{\pm i\phi},\\ {}^{-2}Y_{2\pm2} &= \sqrt{\frac{5}{64\pi}}(1\pm\cos\iota)^2 e^{\pm 2i\phi}. \end{aligned} \tag{8}$$

The root-sum-square strain, $h_{\rm rss}$, is defined as

$$h_{\rm rss} = \left[\int_{-\infty}^{\infty} dt[h_+^2(t;\iota,\phi) + h_\times^2(t;\iota,\phi)]\right]^{1/2}. \tag{9}$$

Using the mode decomposition introduced previously, we construct an explicit angle-dependent expression for $h_{\rm rss}$, which we analytically average over all source angles. Defining

$$\langle h_{\rm rss}\rangle = \iint d\Omega h_{\rm rss}, \tag{10}$$

we obtain

$$\begin{aligned} \langle h_{\rm rss}\rangle = \frac{G}{c^4}\frac{1}{D}\Bigg[\frac{8}{15}\int_{-\infty}^{\infty} dt[&\ddot{I}_{xx}^2 + \ddot{I}_{yy}^2 + \ddot{I}_{zz}^2\\ &- (\ddot{I}_{xx}\ddot{I}_{yy} + \ddot{I}_{xx}\ddot{I}_{zz} + \ddot{I}_{yy}\ddot{I}_{zz})\\ &+ 3(\ddot{I}_{xy}^2 + \ddot{I}_{xz}^2 + \ddot{I}_{yz}^2)]\Bigg]^{1/2}. \end{aligned} \tag{11}$$

A. Numerical waveforms

1. Gravitational waves from convection and SASI

Postbounce CCSN cores are unstable to convection. The stalling shock leaves behind an unstable negative entropy gradient, leading to a burst of prompt convection soon after core bounce. As the postbounce evolution proceeds, neutrino heating sets up a negative entropy gradient in the region of net energy deposition (the gain layer) behind the shock, leading to neutrino-driven convection. Simultaneously, neutrino diffusion establishes a negative lepton gradient in the mantle of the proto-neutron star (NS), leading to proto-NS convection. The GW signal from these convective processes has a broad spectrum. The prompt convection GW emission occurs at frequencies in the range 100–300 Hz, while neutrino-driven convection at later times sources GW emission with significant power at frequencies between ~300–a1000 Hz (increasing with time [12–15]). Proto-NS convection contributes at the highest frequencies ($\gtrsim$1000 Hz). While the frequency content of the signal is robust, the phase is stochastic due to the chaotic nature of turbulence [1,74].

In addition to convection, depending on progenitor structure (and, potentially, dimensionality of the simulation; cf. [29,31,146–148]), the shock front may become unstable to SASI, which leads to large-scale modulations of the accretion flow. This results in sporadic large amplitude spikes in the GW signal when large accreting plumes are decelerated at the edge of the proto-NS (e.g., [12,13]).

We draw sample waveforms for GWs from nonrotating core collapse from the studies of Yakunin *et al.* [14], Müller *et al.* [37], and Ott *et al.* [29]. Yakunin *et al.* performed 2D simulations of neutrino-driven CCSNe. We choose a waveform obtained from the simulation of a $15M_\odot$ progenitor star (referred to as `yak` in the following). Due to axisymmetry, the extracted waveform is linearly polarized. Müller *et al.* performed 3D simulations of neutrino-driven CCSNe with a number of approximations to make the simulations computationally feasible. Importantly, they started their simulations after core bounce and assumed a time-varying inner boundary, cutting out much of the proto-neutron star. Prompt and proto-neutron star convection do not contribute to their waveforms, and higher frequency GW emission is suppressed due to the artificial inner boundary. As the simulations are 3D, the Müller *et al.* waveforms have two polarizations, and we use waveforms of models L15-3, W15-4 (two different $15M_\odot$ progenitors), and N20-2 (a $20M_\odot$ progenitor). We refer to these waveforms as `müller1`, `müller3`, and `müller2`, respectively. Ott *et al.* performed 3D simulations of neutrino-driven CCSNe. The simulations are general-relativistic and incorporate a three-species neutrino leakage scheme. As the simulations are 3D, the Ott *et al.* waveforms have two polarizations, and we use the GW waveform from model $s27f_{\rm heat}1.05$ (a $27M_\odot$ progenitor). We hereafter refer to this waveform as `ott`. We plot the GW signal for the `ott` model in the top panel of Fig. 3.

2. Gravitational waves from rotating core collapse and bounce

Rotation leads to oblateness (an $\ell=2, m=0$ quadrupole deformation) of the inner quasihomologously collapsing core. Extreme accelerations experienced by the inner core at bounce lead to a large spike in the GW signal at bounce, followed by ringdown of the proto-neutron star as it settles to its new equilibrium state (see, e.g., [1,17,149] for a detailed

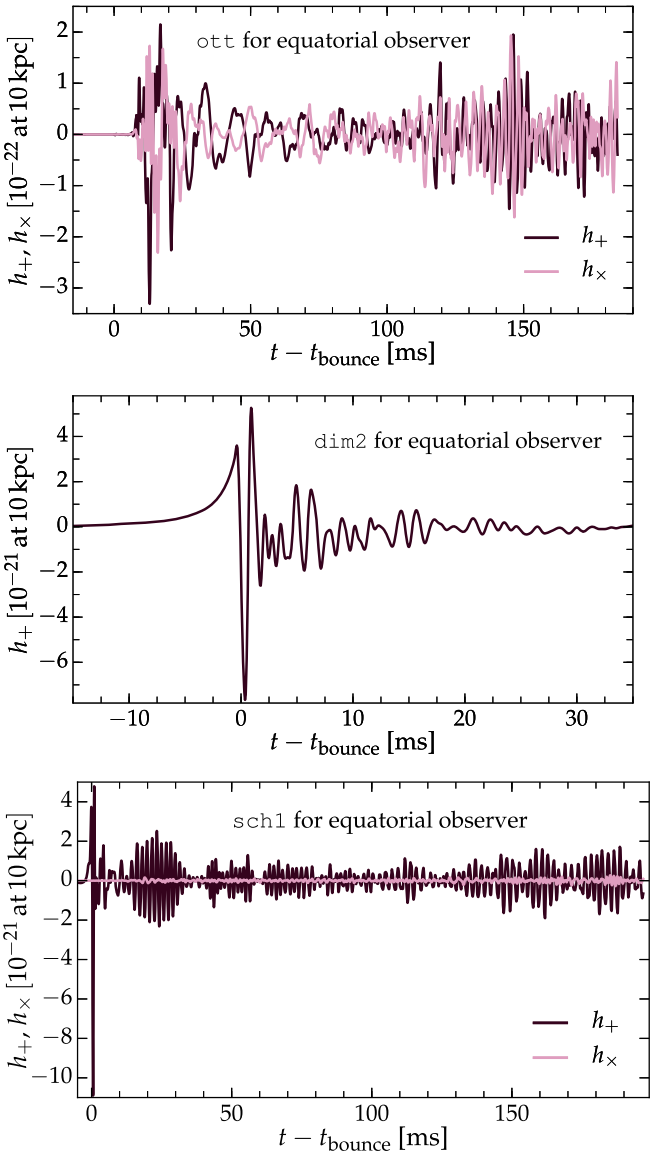

FIG. 3. The time domain GW strain for representative models of convection and standing accretion-shock instability (ott; top panel), bounce and ringdown of the proto-neutron star (dim2; middle panel), and non-axisymmetric rotational instabilities (sch1; bottom panel) as seen by an equatorial ($\iota = \pi/2$; $\phi = 0$) observer at 10 kpc. We note that the typical GW strain from rotating core collapse is roughly an order of magnitude larger than the typical GW strain from neutrino-driven explosions. In addition, the typical GW signal duration of bounce and ringdown of the proto-neutron star is $\sim$ few 10 ms, compared to the typical GW signal duration of $\sim$ few 100 ms for neutrino-driven explosions. Non-axisymmetric rotational instabilities, however, may persist for $\sim$ few 100 ms.

discussion). The GW signal is dependent on the mass of the inner core, its angular momentum distribution, and the equation of state of nuclear matter. There are significant uncertainties in these and it is difficult to exactly predict the time series of the GW signal. Nevertheless, work by several authors [11,16,20,149–152] has demonstrated that GW emission from rotating core collapse and bounce has robust features that can be identified and used to infer properties of the progenitor core.

We draw three sample waveforms from the axisymmetric general-relativistic (conformally flat) simulations of Dimmelmeier *et al.* [17]. All were performed with a 15-$M_\odot$ progenitor star and the Lattimer-Swesty equation of state [153]. The three linearly polarized waveforms drawn from [17], s15A2O05-ls, s15A2O09-ls, and s15A3O15-ls, differ primarily by their initial rotation rate and angular momentum distribution. We refer to them as dim1 (slow and rather uniform precollapse rotation), dim2 (moderate and rather uniform precollapse rotation), and dim3 (fast and strongly differential precollapse rotation), respectively. We plot the GW signal for the dim2 model in the middle panel of Fig. 3.

Shortly after core bounce, nonaxisymmetric rotational instabilities driven by rotational shear (e.g., [38,41,139,143,154]) or, in the limit of extreme rotation, by a classical high-$T/|W|$ instability at $T/|W| \gtrsim 25 - 27\%$ [155], where T is the rotational kinetic energy and W is the gravitational energy, may set in. The nonaxisymmetric deformations may lead to a signficant enhancement of the GW signal from the postbounce phase of rotating CCSNe. We choose two sample waveforms from the 3D Newtonian, magnetohydrodynamical simulations of Scheidegger *et al.* [143], which use a neutrino leakage scheme. All were performed with a 15$M_\odot$ progenitor star, and the Lattimer-Swesty equation of state [153]. Due to the 3D nature of the simulations, the Scheidegger *et al.* waveforms have two polarizations. We employ waveforms for models R3E1AC$_{\rm L}$ (moderate precollapse rotation, toroidal/poloidal magnetic field strength of 10^6G/10^9G), and R4E1AC$_{\rm L}$ (rapid precollapse rotation, toroidal/poloidal magnetic field strength of 10^{12}G/10^9G). We hereafter refer to these waveforms as sch1 and sch2, respectively. We plot the GW signal for the sch1 model in the bottom panel of Fig. 3.

B. Phenomenological waveforms

1. Gravitational waves from long-lived rotational instabilities

Proto-neutron stars with ratio of rotational kinetic energy T to gravitational energy $|W|$, $\beta = T/|W| \gtrsim 25$–27% become dynamically unstable to nonaxisymmetric deformation (with primarily $m = 2$ bar shape). If $\beta \gtrsim 14\%$, an instability may grow on a secular (viscous, GW backreaction) time scale, which may be seconds in proto-neutron stars (e.g., [156]). Furthermore, proto-neutron stars are born differentially rotating (e.g., [157]) and may thus be subject to a dynamical shear instability driving nonaxisymmetric deformations that are of smaller magnitude than in the classical instabilities, but are likely to set in at much lower β. Since this instability operates on differential

rotation, it may last for as long as accretion maintains sufficient differential rotation in the outer proto-neutron star (e.g., [38,139,143,154,158,159] and references therein).

For simplicity, we assume that the net result of all these instabilities is a bar deformation, whose GW emission we model in the Newtonian quadrupole approximation for a cylinder of length l, radius r and mass M in the x–y plane, rotating about the z axis. We neglect spin-down via GW backreaction. The second time derivative of the bar's reduced mass-quadrupole tensor is given by

$$\ddot{I}_{ij} = \frac{1}{6}M(l^2 - 3r^2)\Omega^2 \begin{pmatrix} -\cos 2\Omega t & \sin 2\Omega t \\ \sin 2\Omega t & \cos 2\Omega t \end{pmatrix}, \quad (12)$$

where $\Omega = 2\pi f$ is the angular velocity of the bar (see, e.g., [144] for details). We then obtain the GW signal using the quadrupole formula in Eq. (7) [7,145].

We generate representative analytic bar waveforms by fixing the bar length to 60 km, its radius to 10 km and varying the mass in the deformation M, the spin frequency f, and duration of the bar mode instability Δt. In practice, we scale the waveforms with a Gaussian envelope $\propto \exp(-(t-\Delta t)^2/(\Delta t/4)^2)$ to obtain nearly zero amplitudes at start and end of the waveforms, resulting in waveforms of sine-Gaussian morphology. In this study, we consider three bars of mass $M = 0.2M_\odot$, with $(f, \Delta t) =$ $(400\,\mathrm{Hz}, 0.1\mathrm{s})$, $(400\,\mathrm{Hz}, 1\mathrm{s})$, and $(800\ \mathrm{Hz}, 0.1\mathrm{s})$ (hereafter referred to as `longbar1`, `longbar2`, and `longbar3`, respectively), and three bars of mass $M = 1M_\odot$ with $(f, \Delta t) = (400\ \mathrm{Hz}, 0.1\mathrm{s})$, $(400\ \mathrm{Hz}, 1\mathrm{s})$, and $(800\ \mathrm{Hz}, 0.025\mathrm{s})$ (hereafter referred to as `longbar4`, `longbar5`, and `longbar6`, respectively). We choose these parameters to explore the regime of strong bar-mode GW emission with the constraint that the strongest signal must emit less energy than is available in collapse, $E_{\mathrm{GW}} \lesssim 0.15M_\odot c^2$. Values of $\langle h_{\mathrm{rss}}\rangle$, f_{peak}, and E_{GW} for the six representative waveforms used in this study are shown in Table IV. We plot the GW signal for the `longbar1` model in the top panel of Fig. 4.

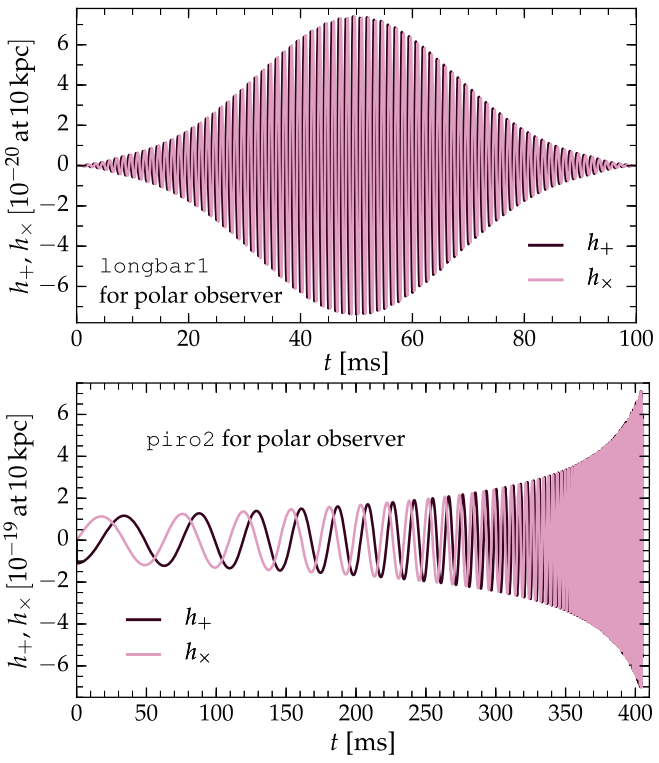

FIG. 4. The time domain GW strain for representative models of bar-mode instability (`longbar1`; top panel) and disk fragmentation instability (`piro2`; bottom panel), as seen by a polar ($\iota = 0$; $\phi = 0$) observer at 10 kpc.

2. Disk fragmentation instability

If the CCSN mechanism fails to reenergize the stalled shock (see, e.g., [160]), the proto-neutron star will collapse to a black hole on a time scale set by accretion (e.g., [161]). Provided sufficient angular momentum, a massive self-gravitating accretion disk/torus may form around the nascent stellar-mass black hole with mass M_{BH}. This scenario may lead to a collapsar-type gamma-ray burst (GRB) or an engine-driven SN [162].

The inner regions of the disk are geometrically thin due to efficient neutrino cooling, but outer regions are thick and may be gravitationally unstable to fragmentation at large radii [43,163]. We follow work by Piro and Pfahl ([43]), and consider the case in which a single gravitationally bound fragment forms in the disk and collapses to a low-mass neutron star with $M_f \sim 0.1 - 1M_\odot \ll M_{\mathrm{BH}}$. We then obtain the predicted GW signal using Eq. (7) [7,145], assuming the fragment is orbiting in the x–y plane, such that

$$\ddot{I}_{ij} = 2\frac{M_{\mathrm{BH}}M_f}{(M_{\mathrm{BH}}+M_f)}r^2\Omega^2 \begin{pmatrix} -\cos 2\Omega t & -\sin 2\Omega t \\ -\sin 2\Omega t & \cos 2\Omega t \end{pmatrix}. \quad (13)$$

For more technical details, including the waveform generation code, we direct the reader to [43,164]. We consider waveforms from four example systems with $(M_{\mathrm{BH}}, M_f) = (5M_\odot, 0.07M_\odot)$, $(5M_\odot, 0.58M_\odot)$, $(10M_\odot, 0.14M_\odot)$, and $(10M_\odot, 1.15M_\odot)$ (hereafter denoted `piro1`, `piro2`, `piro3`, and `piro4`, respectively). Values of $\langle h_{\mathrm{rss}}\rangle$, f_{peak}, and E_{GW} for the four representative waveforms used in this study are shown in Table IV. We plot the GW signal for the `piro2` model in the bottom panel of Fig. 4.

3. Ad hoc signal models

It is possible that there are GW emission mechanisms from CCSNe that we have not considered. In this case, it is instructive to determine the sensitivity of our GW search to short, localized bursts of GWs in time-frequency space. For this reason, we include *ad hoc* signal models in our signal injections, in addition to the aforementioned physically motivated signal models. We take motivation from the all-sky, all-time searches for GW bursts performed in the intial

TABLE V. Key characteristics of the *ad hoc* sine-Gaussian waveforms employed in this study. f_0 is the central frequency, Q is the quality factor, and α is the ellipticity. See Eq. (14) in Sec. IV B 3 for details.

Model name	f_0 [Hz]	Q	α
sglin1, sgel1	70	3	0,1
sglin2, sgel2	70	9	0,1
sglin3, sgel3	70	100	0,1
sglin4, sgel4	100	9	0,1
sglin5, sgel5	153	9	0,1
sglin6, sgel6	235	3	0,1
sglin7, sgel7	235	9	0,1
sglin8, sgel8	235	100	0,1
sglin9, sgel9	361	9	0,1
sglin10, sgel10	554	9	0,1
sglin11, sgel11	849	3	0,1
sglin12, sgel12	849	9	0,1
sglin13, sgel13	849	100	0,1
sglin14, sgel14	1053	9	0,1
sglin15, sgel15	1304	9	0,1

detector era [59,165], and consider linearly and elliptically polarized sine-Gaussian GW bursts. Characterized by central frequency, f_0, and quality factor, Q, the strain is given by

$$h_+(t) = A\left(\frac{1+\alpha^2}{2}\right)\exp(-2\pi f_0^2 t^2/Q^2)\sin(2\pi f_0 t),$$
$$h_\times(t) = A\alpha\exp(-2\pi f_0^2 t^2/Q^2)\cos(2\pi f_0 t), \quad (14)$$

where A is some common scale factor, and α is the ellipticity, where $\alpha = 0$ and 1 for linearly and circularly polarized waveforms, respectively. Assuming isotropic energy emission, we may compute the energy in GWs associated with a sine-Gaussian burst as

$$E_{\rm GW} = \frac{\pi^2 c^3}{G} d^2 f_0^2 h_{\rm rss}^2, \quad (15)$$

where d is the distance at which $h_{\rm rss}$ is computed. In Table V, we list the f_0, Q, and α values for all sine-Gaussian waveforms considered in this study.

V. DATA ANALYSIS METHODS

A. X-Pipeline: A search algorithm for gravitational wave bursts

X-Pipeline is a coherent analysis pipeline used to search for GW transient events associated with CCSNe, gamma-ray bursts (GRBs), and other astrophysical triggers. X-Pipeline has a number of features designed specifically to address the challenges discussed in Sec. II. For example, since the signal duration is uncertain, X-Pipeline uses multiresolution Fourier transforms to maximize sensitivity across a range of possible signal durations. The pixel clustering procedure applied to time-frequency maps of the data is designed to find arbitrarily shaped, connected events [166]. The potentially nonstationary data is whitened in blocks of 256 s duration, removing the effect of variations in background noise levels which typically happen on longer time scales. Short-duration noise glitches are removed by comparing measures of interdetector correlations to a set of thresholds that are tuned using simulated GW signals from the known sky position of the CCSNe and actual noise glitches over the on-source window. The thresholds are selected to satisfy the Neyman-Pearson optimality criterion (maximum detection efficiency at fixed false-alarm probability), and are automatically adjusted for the event amplitude to give robust rejection of loud glitches. We provide a brief overview of the functionality of X-Pipeline here, specifically in the context of CCSN searches, and direct the reader to the X-Pipeline technical document for a more in-depth description [78].

As previously introduced in Sec. III B, an external EM or neutrino trigger at time t_0 can be used to define an astrophysically motivated on-source window, such that the expected GW counterpart associated with the external trigger is enclosed within the on-source window. For the purposes of this study, we choose four distinct on-source windows centered about t_0—see Sec. III B for detailed information. Given a specified external source location, (α, δ), the N data streams observed from an N-detector network are time-shifted, such that any GW signals present will arrive simultaneously in each detector. The time-shifted data streams are then projected onto the dominant polarization frame, in which GW signals are maximized, and null frame, in which GW signals do not exist by construction [167,168].

The data streams in the dominant polarization frame are processed to construct spectrograms, and the 1% of time-frequency pixels with the largest amplitude are marked as candidate signal events. For each cluster, a variety of information on the time and frequency characteristics is computed, in addition to measures of cluster significance, which are dependent on the total strain energy $|h|^2$, of the cluster. For the purposes of this study, a Bayesian likelihood statistic is used to rank the clusters. We direct the reader to [64,78] for a detailed discussion of the cluster quantities used by X-Pipeline.

For statements on the detection of GWs to be made, we must be able to show with high confidence that candidate events are statistically inconsistent with the background data. To do this, we consider the loudest event statistic, where the loudest event is the cluster in the on-source with the largest significance; we hereafter denote the significance of the loudest event $\mathcal{S}^{\rm on}_{\rm max}$ [169,170]. We estimate the cumulative distribution of the loudest significances of background events, $\mathcal{C}(\mathrm{S}_{\rm max})$, and set a threshold on the false alarm probability (FAP)

that the background could produce an event cluster in the on-source with significance $\mathcal{S}^{\rm on}_{\rm max}$. If $\mathcal{C}(\mathrm{S}^{\rm on}_{\rm max})$ is greater than the threshold imposed, we admit the loudest event as a potential GW detection candidate. For the purposes of this study, we impose FAP $= 0.1\%$, which corresponds to $\sim 3.3\sigma$ confidence.

For Gaussian noise, the significance distribution of background events can be estimated analytically, but as mentioned in Sec. II C, glitches produce excess-power clusters in the data that may be mistaken for a GW event. However, the method used by `X-Pipeline` to construct the dominant polarization frame results in strong correlations between the incoherent energy I (from the individual data streams) and the coherent energy E (from the combined data streams) for glitches [171]. A comparison of I and E for candidate events can thus be used to *veto* events that have the same statistical properties as the background noise. A threshold curve in (I, E) space is defined, and veto tests may be one-sided (all events on one side of the curve are vetoed), or two-sided (events within some band centered on the $I = E$ diagonal are vetoed). The threshold curve is chosen to optimize the ratio of glitch rejection to signal acceptance.

In practice, the statistics of the distribution of background events in the data are determined by applying unphysically large time-shifts, hereafter referred to as "lags," to the detector streams. Additionally, we generate known signal events by injecting simulated GW signals into the data streams. The background and signal events are split into two sets, used for pipeline *tuning* and testing detection performance, respectively. A large range of trial threshold cuts are applied for the background rejection test, and the statistics of the background events computed. The minimum injection amplitude for which 50% of the injections (1) survive the threshold cuts and (2) have a FAP $\leq 0.1\%$, $h^{50\%}_{\rm rss}$, for a given family of GW signal models is computed. This is known as the *upper limit* on $h_{\rm rss}$ at 50% confidence—see Sec. V D. The optimal threshold cut is defined as that for which $h^{50\%}_{\rm rss}$ is minimized at the specified FAP. Unbiased statements on the background distribution and waveform detectability can then be made by processing the tuning set events with the thresholds obtained previously.

B. Recoloring of GW detector data

The many methods used to detect GW transients can often be proven to be near optimal in the case of stationary, Gaussian noise. Data from the GW detectors, however, is not expected to be stationary or Gaussian, and as such, it is important to test the efficacy of one's detection method in nonstationary and non-Gaussan noise. To this end, we utilize observational data taken by the Hanford and Livingston LIGO detectors during the S5 science run, in addition to data taken by the Virgo detector during the VSR1 science run. The S5 data is now publically available via the LIGO Open Science Center (LOSC) [172]. Recoloring of these data to the predicted power spectral densities (PSDs) of the Advanced detectors during different stages during the next five years (see Sec. III C) permits a more realistic estimation of the sensitivity of the advanced detectors to CCSNe.

We recolor the GW data using the `gstlal` software packages [173,174], following the procedure outlined below:

(i) Determine PSD of original data.
(ii) Whiten data using a zero-phase filter created from the original PSD.
(iii) Recolor whitened data to desired PSD.

This method provides non-Gaussian, nonstationary detector data including noise transients, tuned to any sensitivity desired. For specific details on the detector networks, and noise PSDs considered, see Sec. III C. For the purposes of this study, we recolor 100 hours of data from the H1 and L1 detectors during the S5 science run, and the V1 detector during the VSR1 science run.

C. Injection of known signal events

As mentioned previously in Sec. V A, it is a well-established practice to inject known signal events into detector data for analysis (see, e.g., [175]). This process permits the estimation of detection efficiency for GWs from signal models of varying time-frequency characteristics.

A GW source can be characterized by five angles—$(\iota, \phi; \theta, \Phi, \psi)$, where (θ, Φ, ψ) describe the sky location and polarization of the source, while (ι, ϕ) describe the internal orientation of the source relative to the line of sight of the observer. In this study, the source location in Earth-centered coordinates (θ, Φ) are fixed by right ascension α, and declination δ of the source, in addition to the GPS time at geocenter of the injected signal—see Sec. III for more detailed information. The polarization angle ψ relating the source and detector reference frames is distributed uniformly in $[0, 2\pi]$ for all injections. For CCSN systems, it is not possible to know the inclination angle ι and azimuthal angle ϕ. To represent this, we inject signals with many different (ι, ϕ), to average over all possible internal source orientations.

As mentioned previously in Sec. IV, we may construct the strain for different internal source orientations by projecting the mode coefficients $H_{lm}(t)$ onto the -2 spin-weighted spherical harmonics, ${}^{-2}Y_{lm}(\iota, \phi)$. Making use of geometric symmetries for different astrophysical systems permits the use of polarization factors to describe $h_{+,\times}(\iota, \phi)$ as a function of $h_{+,\times;0} = h_{+,\times}(\iota = 0, \phi = 0)$. Defining polarization factors $n_{+,\times}(\iota, \phi)$, we may write the strain at an arbitrary internal orientation as

$$h_+(\iota, \phi) = n_+(\iota, \phi) h_{+;0}, \tag{16}$$

$$h_\times(\iota, \phi) = n_\times(\iota, \phi) h_{\times;0}, \tag{17}$$

where the form of $n_{+,\times}(\iota,\phi)$ is dependent on the symmetries of the system considered.

For linearly polarized signals (e.g., linear sine-Gaussian injections), we apply

$$n_{+}^{\mathrm{lin}} = 1, \tag{18}$$

$$n_{\times}^{\mathrm{lin}} = 0. \tag{19}$$

For elliptically polarized signals (e.g., bar-mode instability, disk fragmentation instability, and elliptical sine-Gaussian injections), we apply

$$n_{+}^{\mathrm{el}} = \frac{1}{2}(1+\cos\iota)^2, \tag{20}$$

$$n_{\times}^{\mathrm{el}} = \cos\iota. \tag{21}$$

For the 2D CCSN emission models, the axisymmetric system results in a linearly polarized GW signal. The system has azimuthal symmetry, resulting in zero amplitude for all GW modes except H_{20}. From Eq. (6), we see that the strain h_{+} varies with ι as

$$h_{+}(\iota) = h_{+}^{\mathrm{eq}}\sin^2\iota,$$

where h_{+}^{eq} is the strain as seen by an equatorial observer. We are thus able to apply SN polarization factors:

$$n_{+}^{\mathrm{SN}} = \sin^2\iota,$$
$$n_{\times}^{\mathrm{SN}} = 0.$$

For the 3D CCSN emission models, the GW polarizations are nontrivially related to the internal source angles, and as such, the h_{+} and $h_{\times}$ strains must be computed for specific internal configurations using Eq. (6). No additional polarization factors are applied for these waveforms.

For all emission models for which $n_{+,\times}$ can be defined, we inject signals uniform in $\cos\iota \in [-1,1]$. For the 3D CCSN emission models, we inject signals uniformly drawn from a bank of 100 realizations of $(\cos\iota,\phi)$, where $\cos\iota \in [-1,-7/9,\ldots,1]$ and $\phi \in [0,2\pi/9,\ldots,2\pi]$.

For each observational scenario, we inject 250 injections across the considered on-source window.

D. Upper limits and detection efficiencies

To make detection statements and set upper limits on the GWs emitted from CCSNe, we must compare the cumulative distribution of background event significance, $\mathcal{C}(\mathcal{S}_{\mathrm{max}})$, estimated from off-source data, to the maximum event significance in the on-source data $\mathcal{S}_{\mathrm{max}}^{\mathrm{on}}$. If no on-source events are significant, we may instead proceed to set frequentist upper limits on the GWs from the CCSN of interest, given the emission models considered.

As alluded to previously in Sec. V A, we may define the 50% confidence level upper limit on the signal amplitude for a specific GW emission model as the minimum amplitude for which the probability of observing the signal, if present in the data, with a cluster significance louder than $\mathcal{S}_{\mathrm{on}}^{\mathrm{max}}$ is 50%. In this study, we aim to determine the 50% upper limit, as defined here, as a function of

(i) Source distance $d^{50\%}$, in the context of astrophysically motivated signal models.
(ii) Root-sum-square amplitude $h_{\mathrm{rss}}^{50\%}$, in the context of linear and elliptical sine-Gaussian waveforms. It is more relevant, astrophysically to consider the corresponding 50% upper limit on the energy emitted in GWs, $E_{\mathrm{GW}}^{50\%}$, which we compute from $h_{\mathrm{rss}}^{50\%}$ using Eq. (15).

After the on-source data has been analyzed and $\mathcal{S}_{\mathrm{on}}^{\mathrm{max}}$ computed, we inject a large number of known signal events for families of waveforms for which $h_{\mathrm{rss}}^{50\%}$ and $d^{50\%}$ (where applicable) are desired. For a single waveform family, we outline the upper limit procedure:

(i) Inject many waveforms at different times during the on-source window and with a broad range of polarization factors.
(ii) Compute the largest significance $\mathcal{S}$ of any clusters associated with the injected waveforms (observed within 0.1 seconds of the injection time) that have survived after application of veto cuts.
(iii) For all injections, compute the percentage of injections for which $\mathcal{S} > \mathcal{S}_{\mathrm{on}}^{\mathrm{max}}$. This is called the "detection efficiency," $\mathcal{E}$.
(iv) Repeat procedure, modifying the injection amplitude of each waveform by a scaling factor.

The final goal is to produce a plot of the detection efficiency as a function of h_{rss} or distance d for each waveform family, such that one may place upper limits on the GW emission models considered. From the efficiency curve, one may determine $h_{\mathrm{rss}}^{50\%}$ as

$$\mathcal{E}(h_{\mathrm{rss}} = h_{\mathrm{rss}}^{50\%}) = 0.5. \tag{22}$$

Given an astrophysical signal injected at $h_{\mathrm{rss}}^{\mathrm{inj}}$ corresponding to fiducial distance d^{inj}, we may define $d^{50\%}$ as

$$d^{50\%} = \left(\frac{h_{\mathrm{rss}}^{50\%}}{h_{\mathrm{rss}}^{\mathrm{inj}}}\right) d^{\mathrm{inj}}. \tag{23}$$

We note that X-Pipeline rescales the detection efficiency to account only for injections placed at times at which detector data is available. Without this correction, the efficiencies computed asymptote to the duty cycle fraction for the on-source window considered. For the data considered in this study, the total duty cycle is typical of the S5 and VSR1 science runs, which is described in detail in Sec. II B.

E. Systematical uncertainties

The uncertainties in the efficiencies, upper limits and exclusion capabilities of our analysis method are related to

non-Gaussian transients in the data, in addition to calibration uncertainties. There are a number of systematic uncertainties present in this study that will non-negligibly affect the results. We consider only a short period of recolored data from LIGO's S5 and Virgo's VSR1 data-taking runs, over which the frequency and character of non-Gaussian transients changed non-negligibly. The noise transients in advanced LIGO data are also significantly different to those in initial LIGO data, and the non-Gaussianities are not yet understood well enough to make quantitative statements on the statistical behavior of the data. For these reasons, we only quote results to two significant figures in this study. The statistical uncertainty in detector calibration can be characterized by the 1σ statistical uncertainty in the amplitude and phase of the signal. Uncertainties in phase calibration can be estimated by simulating its effect on the ability to recover test injections. We direct the reader to Kalmus [176], in which it is shown that phase uncertainties contribute negligibly to the total systematic error, and thus we only consider amplitude uncertainties in this study. The target design amplitude uncertainties in the frequency range 40–2048 Hz for Advanced LIGO and Advanced Virgo are 5% at 2σ confidence [177]. As such, the upper limits for $h_{\mathrm{rss}}^{50\%}$ and $d^{50\%}$ obtained from a search for GWs from CCSNe in the Advanced detector era will have intrinsic ∼5% uncertainties. For comparison, typical amplitude uncertainties due to calibration in S5 were below 15% [98].

VI. RESULTS

In this section, we present the results for the detectability of the considered GW emission models described in Sec. IV.

We consider realistic waveform models from numerical simulations of core collapse. For the 'garden-variety' CCSN models considered (`müller1`, `müller2`, `müller3`, `ott`, and `yak`), convection and SASI are the dominant GW emission processes. For rotating core collapse, we choose models where bounce and ringdown of the proto-neutron star (`dim1`, `dim2`, and `dim3`), and nonaxisymmetric rotational instabilities (`sch1` and `sch2`) are the dominant GW emission processes. As these waveforms will only be detectable from CCSNe at close distances ($d \lesssim 100$ kpc), we consider CCSNe in the direction of the Galactic center and LMC, for which the coincident neutrino signal will be detected. We use a conservative on-source window of $[-10, +50]$ s about the time of the initial SNEWS trigger.

For more distant CCSNe, we consider more speculative, extreme phenomenological GW emission models for long-lived bar-mode instabilities (`longbar1`, `longbar2`, `longbar3`, `longbar4`, `longbar5`, and `longbar6`) and disk fragmentation instabilities (`piro1`, `piro2`, `piro3`, and `piro4`). More distant CCSNe will not be detectable via neutrinos, but the EM counterpart will be observed. We consider CCSNe in M31 and M82, and use on-source windows assuming a compact, stripped progenitor star of 61 minutes and 24 hour 1 minute, respectively. For an extended, red supergiant progenitor, we use on-source windows of 51 hours and 74 hours for M31 and M82, respectively.

For all host galaxies, we consider *ad hoc* sine-Gaussian bursts to assess the sensitivity of our analysis to localized bursts of energy in time-frequency space.

We remind the reader of the large systematic uncertainties associated with these results and, as such, quote all results to two significant figures.

A. Numerical waveforms

We present the distances $d^{50\%}$ at which 50% detection efficiency is attained (the measure we use for 'detectability') for the considered numerical waveforms in Table VI, for CCSNe in the direction of the Galactic center and LMC, in the context of a 60-second on-source window.

For CCSNe in the direction of the Galactic center, we see that emission from neutrino-driven convection and SASI is detectable out to ∼(1.0–2.4) kpc with the `HL 2015`

TABLE VI. The distance in kpc at which 50% detection efficiency is attained, $d^{50\%}$ for the numerical core-collapse emission models considered using the `HL 2015`, `HLV 2017`, and `HLV 2019` detector networks, for CCSNe in the direction of the Galactic center and the LMC.

	$d^{50\%}$ [kpc] for Galactic center			$d^{50\%}$ [kpc] for LMC		
Waveform	`HL 2015`	`HLV 2017`	`HLV 2019`	`HL 2015`	`HLV 2017`	`HLV 2019`
`müller1`	2.3	3.3	4.7	2.5	3.8	5.3
`müller2`	1.0	1.5	2.2	1.2	1.8	2.5
`müller3`	1.2	1.5	2.4	1.4	1.6	2.7
`ott`	2.4	3.4	5.5	3.2	4.9	7.2
`yak`	1.5	1.8	5.1	1.6	2.1	6.2
`dim1`	7.0	9.1	17	7.4	10	18
`dim2`	11	17	29	13	20	32
`dim3`	13	21	38	18	32	50
`sch1`	31	43	78	36	48	90
`sch2`	35	50	98	45	56	120

detector network. This increases to ∼(1.5–3.4) kpc and ∼(2.2–5.5) kpc with the HLV 2017 and HLV 2019 detector networks, respectively.

Similarly, we see that emission from bounce and ringdown of the central proto-neutron star core is detectable out to ∼(7.0–13.4) kpc for CCSNe in the direction of the Galactic center with the HL 2015 detector network. This increases to ∼(9.1–21) kpc and ∼(17–38) kpc with the HLV 2017 and HLV 2019 detector networks, respectively.

Emission from nonaxisymmetric rotational instabilities from CCSNe in the direction of the Galactic center is detectable out to ∼(31–35) kpc with the HL 2015 detector network. This increases to ∼(43–50) kpc and ∼(78–98) kpc with the HLV 2017 and HLV 2019 detector networks, respectively.

Assuming the fiducial distance of a galactic CCSN to be ∼9 kpc, this suggests that we will be able to detect emission from the more extremely rapidly rotating CCSN waveforms considered with the HL 2015 detector network, while all considered rapidly rotating waveforms will be detectable for CCSNe in the direction of the Galactic center with the HLV 2017 and HLV 2019 detector networks. We will be limited to detection of nonrotating CCSNe within 5.5 kpc with the most sensitive HLV 2019 detector network.

Considering CCSNe in the direction of the LMC, we see that emission from neutrino-driven convection and SASI is detectable out to ∼(1.2–3.2) kpc with the HL 2015 detector network. This increases to ∼(1.6–4.9) kpc and ∼(2.5–7.2) kpc with the HLV 2017 and HLV 2019 detector networks, respectively. Given that the LMC is ∼50 kpc away, this shows that emission from neutrino-driven convection and SASI will not be detectable from CCSNe in the LMC.

Emission from bounce and ringdown of the central proto-neutron star core is detectable out to ∼(7.4–18) kpc and ∼(11–32) kpc for CCSNe in the direction of the LMC with the HL 2015 and HLV 2017 detector networks, respectively. This increases to ∼(18–50) kpc with the HLV 2019 detector network. This suggests that emission from the bounce and subsequent ringdown of the proto-neutron star may not be detectable from CCSNe in the LMC for even the most rapidly rotating waveform considered with the HLV 2019 detector network.

We see that emission from nonaxisymmetric rotational instabilities from CCSNe in the direction of the LMC is detectable out to ∼(36–45) kpc with the HL 2015 detector network. This increases to ∼(48–56) kpc and ∼(90–120) kpc with the HLV 2017 and HLV 2019 detector networks, respectively. This suggests we will be able to detect emission from nonaxisymmetric rotational instabilities for CCSNe in the LMC with the HLV 2017 detector network.

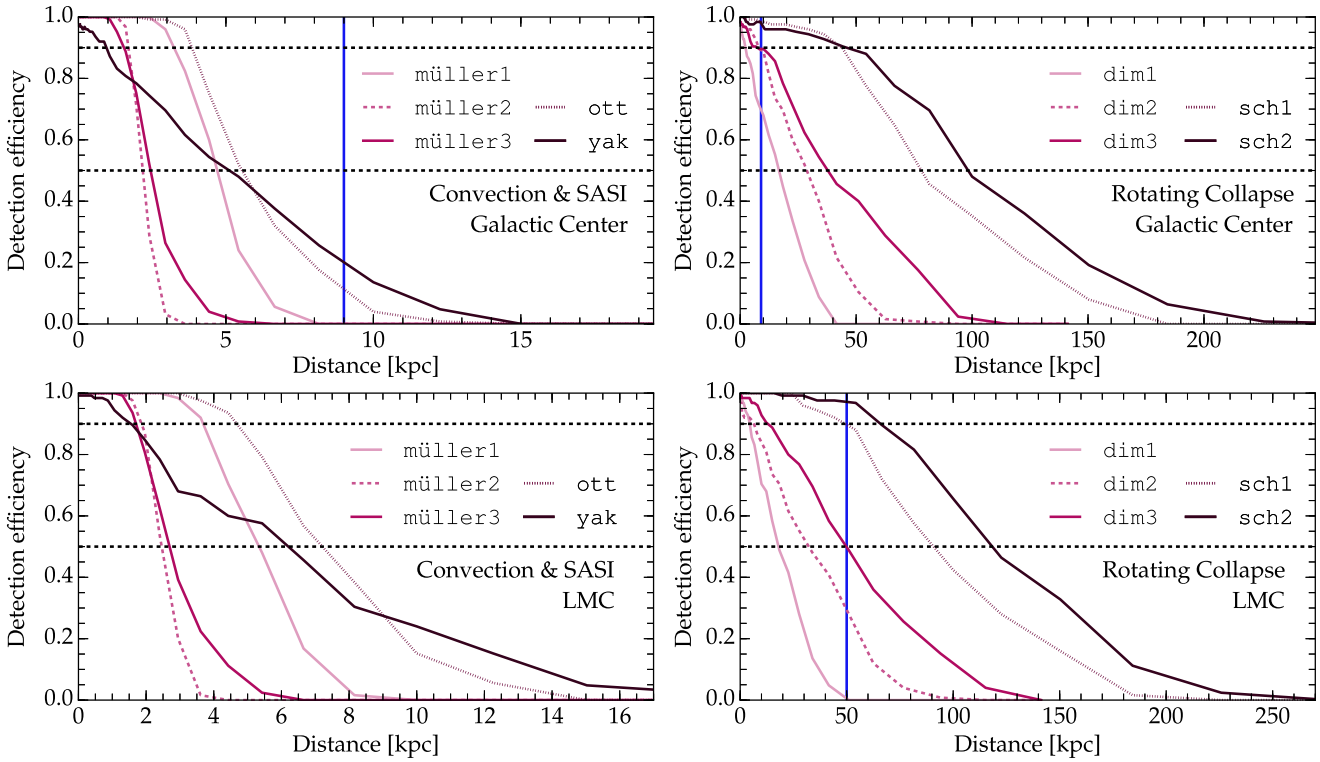

FIG. 5. The detection efficiency as a function of distance for the numerical waveforms in this study, in the context of a 1 minute on-source window and the HLV 2019 detector network. The top row is for galactic sources, and the bottom row is for sources in the Large Magellanic Cloud. In each plot, 50% and 90% detection efficiency is marked with a dashed black line, and the distance to the host galaxy is marked with a vertical blue line.

Figure 5 presents the detection efficiency as a function of distance, for the numerical waveforms considered, for CCSNe directed toward the Galactic center and the LMC.

B. Extreme phenomenological models

We present the distances at which 50% detection efficiency is attained $d^{50\%}$ (the measure we use for "detectability") for the considered phenomenological waveforms in Table VII, for CCSNe in the direction of M31, in the context of 61-minute and 51-hour on-source windows, and M82, in the context of 24-hour 1-minute and 74-hour on-source windows.

For CCSNe in the direction of M31, we see that emission from long-lived bar-mode instabilities will be detectable out to ∼(0.5–5.2) Mpc [∼(0.2–2.7) Mpc] when using a 61-minute [51-hour] on-source window, with the HL 2015 detector network. The distances at which 50% detection efficiency is reached, $d^{50\%}$, increase to ∼(0.8–8.6) Mpc [∼(0.3–3.4) Mpc] and ∼(1.6–18) Mpc (∼(0.8–9.9) Mpc) when using a 61-minute [51-hour] on-source window, with the HLV 2017 and HLV 2019 detector networks, respectively.

Emission from disk fragmentation instabilities will be detectable out to ∼(0.9–12) Mpc [∼(0.6–6.5) Mpc] and ∼(1.3–19) Mpc [∼(0.6–6.1) Mpc] when using 61-minute [51-hour] on-source windows with the HL 2015 and HLV 2017 detector networks, respectively, for CCSNe in the direction of M31. These distances increase to ∼(2–28) Mpc [∼(1.4–18) Mpc] when using a 61-minute [51-hour] on-source window, with the HLV 2019 detector network.

Assuming a fiducial distance of 0.77 Mpc for a CCSN in M31, this suggests that we will be able to detect emission from all considered long-lived bar-mode instability waveforms with the HLV 2019 detector network, while the detectable fraction of considered waveforms with the HL 2015 and HLV 2017 detector networks is strongly dependent on the on-source window length. Taking the 51-hour on-source window as the most pessimistic scenario, ∼50% and ∼67% of the considered bar-mode instability waveforms are detectable with the HL 2015 and HLV 2017 detector networks, respectively.

Similarly, emission from the considered disk fragmentation instabilities waveforms will be detectable for a CCSN in M31 with the HLV 2019 detector network for all considered on-source windows. For the 51-hour on-source window, we see that ∼75% of the considered disk-fragmentation instability waveforms are detectable with both the HL 2015 and HLV 2017 detector networks.

We note that, for some models, the $d^{50\%}$ values computed for the M31 source, when using a 51-hour on-source window, are smaller for the HLV 2017 detector network than the HL 2015 network. While this might at first seem counter-intuitive, this is due to the requirement for coincident data between detectors to run a *coherent* analysis. The lower sensitivity of the HV and LV detectors for the data analyzed, compared with the sensitivity of the HL detectors, reduces the effective total sensitivity of the network. We include the third detector, however, as it increases the overall duty cycle of the network.

For CCSNe in the direction of M82, we see that emission from long-lived bar-mode instabilities will be detectable out to ∼(0.3–3) Mpc [∼(0.4–4.3) Mpc] and ∼(0.3–3.4) Mpc [∼(0.4–5.2) Mpc] using a 24 hour 1 minute [74 hour] on-source window, with the HL 2015 and HLV 2017 detector networks. This increases to ∼(1–9.7) Mpc [∼(0.7–8.3) Mpc] for a 24 hour 1 minute [74 hour] on-source window, with the HLV 2019 detector network.

For emission from disk fragmentation instabilities for CCSNe in the direction of M82, the distance reach is ∼(0.5–6.4) Mpc [∼(0.7–7.5) Mpc] when using a 24-hour 1-minute [74-hour] on-source window with the HL 2015 detector network. This increases to ∼(0.7–8.6) Mpc [∼(0.8–9.5) Mpc] and ∼(1.3–16) Mpc [∼(1.3–15) Mpc] for the HLV 2017 and HLV 2019 detector networks, respectively.

TABLE VII. The distance in Mpc at which 50% detection efficiency is attained, $d^{50\%}$ for the numerical core-collapse emission models considered using the HL 2015, HLV 2017, and HLV 2019 detector networks, for CCSNe in the direction of M31 and M82, in the context of 61-minute (51-hour) and 24-hour 1-minute (74-hour) on-source windows, respectively.

	$d^{50\%}$ [Mpc] for M31			$d^{50\%}$ [Mpc] for M82		
Waveform	HL 2015	HLV 2017	HLV 2019	HL 2015	HLV 2017	HLV 2019
longbar1	0.5 [0.2]	0.8 [0.3]	1.6 [0.8]	0.3 [0.4]	0.3 [0.4]	1.0 [0.7]
longbar2	1.5 [0.7]	2.5 [0.9]	4.8 [2.8]	0.9 [1.1]	1.0 [1.2]	3.0 [2.1]
longbar3	1.0 [0.6]	1.6 [0.6]	3.6 [2.2]	0.8 [0.8]	0.7 [0.8]	2.4 [1.8]
longbar4	2.0 [1.1]	2.8 [1.2]	6.0 [3.8]	1.1 [1.5]	1.4 [1.5]	3.9 [2.8]
longbar5	5.2 [2.7]	8.6 [3.4]	18 [9.9]	3.0 [4.3]	3.4 [5.2]	9.7 [8.3]
longbar6	2.1 [1.1]	3.4 [1.1]	6.7 [4.7]	1.4 [1.9]	1.4 [1.7]	4.4 [3.7]
piro1	0.9 [0.6]	1.3 [0.6]	2.0 [1.4]	0.5 [0.7]	0.7 [0.8]	1.3 [1.3]
piro2	3.9 [2.2]	6.3 [2.6]	9.4 [5.8]	2.2 [3.2]	3.0 [3.8]	5.7 [5.8]
piro3	1.9 [1.3]	3.4 [1.8]	4.9 [3.7]	1.1 [1.3]	1.5 [1.9]	2.8 [3.1]
piro4	12 [6.5]	19 [6.1]	28 [18]	6.4 [7.5]	8.6 [9.5]	16 [15]

Given a fiducial distance of ∼3.52 Mpc for CCSNe in M82, we note that only the most extreme waveform considered for both long-lived bar-mode instabilities and disk fragmentation instabilities are detectable with the HL 2015 detector network. Of the considered long-lived bar-mode instability waveforms, only the most extreme emission model is detectable with the HLV 2017 detector network, while 50% of the waveforms will be detectable with the HLV 2019 detector network. For emission from disk-fragmentation instabilities, we see that only 50% of the waveforms considered will be detectable out to M82 with the HLV 2017 and HLV 2019 detector networks.

We note that the distance reach for these models increases with the larger on-source window for the M82 source. This is due to the properties of the data over the two considered on-source windows. As previously mentioned, real data from GW detectors is not stationary, and as such, the PSD of the data is a function of time. Time periods over which the detector data is glitchy will have locally have significantly decreased sensitivity when compared to a much larger time period over which the detector is more well behaved. This means that if the on-source window derived happens to lie in a glitchy period of detector data, the sensitivity of the detector network will, unfortunately, be decreased. In repeating the search for a larger on-source window, over which the average sensitivity is much greater, the distance reach for the emission models considered may appear to increase. The detectability of the waveforms considered in this study is established by injecting a number of waveforms over the full on-source window considered. The distance reach for the longer on-source window in this case appears to increase because we inject waveforms uniformly across the on-source window, meaning that many "test" signals are placed at times in the data stretch where the sensitivity is greater, in addition to the shorter, more glitchy, time period where the sensitivity is not as great. This is a great example of how realistic noise can significantly affect the detectability of GWs from CCSNe at different times, and is motivation for improving active noise suppression techniques for the detectors.

Figures 6 and 7 present the detection efficiency as a function of distance for the considered phenomenological extreme emission models, for CCSNe in the direction of M31 and M82 for the HLV 2019 detector network, using on-source windows motivated by type Ibc and Type II CCSNe, respectively.

C. Sine-Gaussian waveforms

The energy emitted in GW, $E_{\rm GW}^{50\%}$, required to attain the root-sum-squared strain at 50% detection efficiency, $h_{\rm rss}^{50\%}$, for the sine-Gaussian bursts considered is presented in

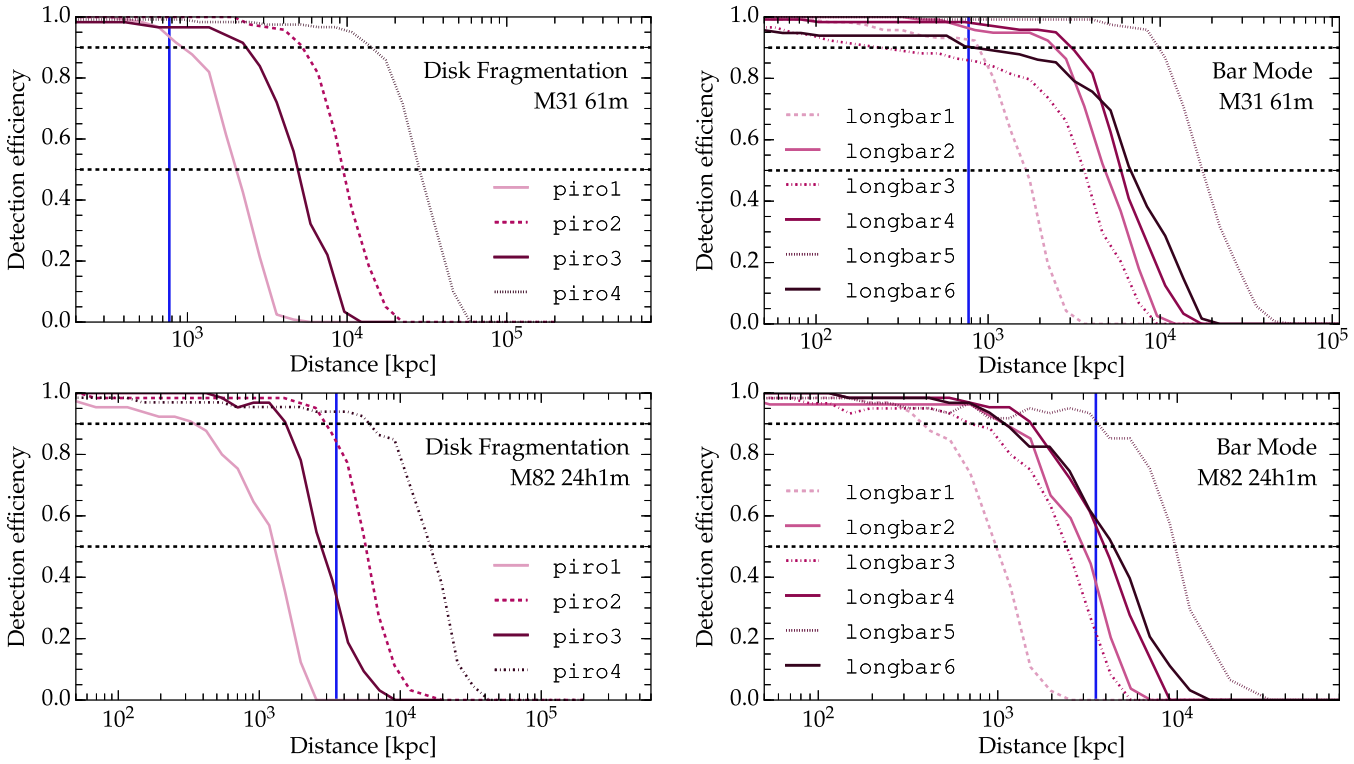

FIG. 6. The detection efficiency as a function of distance for the phenomenological waveforms considered in this study, in the context of the on-source window astrophysically motivated by a stripped envelope type Ibc SN progenitor and the HLV 2019 detector configuration. The top row is for sources in M31 with an on-source window of 61 minutes, and the bottom row is for sources in M82 with a 24-hour 1-minute on-source window. In each plot, 50% and 90% detection efficiency is marked with a dashed black line, and the distance to the host galaxy is marked with a vertical blue line.

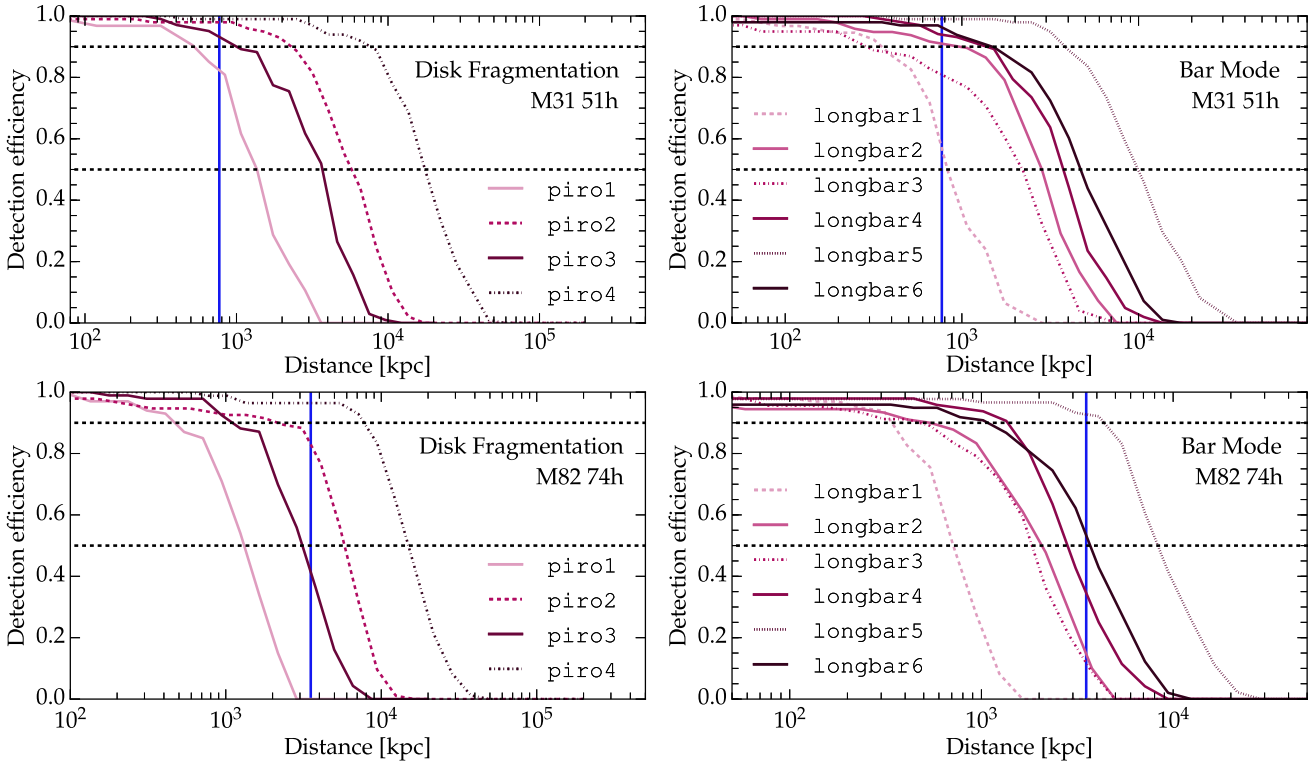

FIG. 7. The detection efficiency as a function of distance for the phenomenological waveforms considered in this study, in the context of the on-source window astrophysically motivated by a type II SN progenitor and the HLV 2019 detector configuration. The top row is for sources in M31 with an on-source window of 51 hours, and the bottom row is for sources in M82 with a 74-hour on-source window. In each plot, 50% and 90% detection efficiency is marked with a dashed black line, and the distance to the host galaxy is marked with a vertical blue line.

Fig. 8 for sources in the direction of the Galactic center, LMC, M31, and M82.

For the *ad hoc* sine-Gaussian bursts considered, we use $E_{\rm GW}^{50\%}$ as the figure of merit for detection.

For CCSNe in the direction of the Galactic center, we see that the typical $E_{\rm GW}^{50\%}$ values are $\sim(8\text{–}110)\times10^{-10}M_{\odot}$ for sine-Gaussian bursts with central frequencies of $\sim(554\text{–}1304)$ Hz, the typical frequencies of emission for CCSNe, using a 60-second on-source window with the HLV 2019 detector network. For CCSNe in the direction of the LMC, we find $E_{\rm GW}^{50\%}\sim(1\text{–}20)\times10^{-8}M_{\odot}$ in the same frequency range. We remind the reader that for the numerical waveforms considered, $E_{\rm GW}\sim(0.1\text{–}4000)\times10^{-10}M_{\odot}$. This is consistent, as X-Pipeline is more sensitive to sine-Gaussian bursts, and we find that only the more rapidly rotating models considered are detectable.

For CCSNe in the direction of M31, we find typical $E_{\rm GW}^{50\%}$ values of $\sim(7\text{–}100)\times10^{-6}M_{\odot}$ across the frequency range considered, using a 51-hour on-source window with the HLV 2019 detector network. For CCSNe in the direction of M82, we find $E_{\rm GW}^{50\%}\sim(3\text{–}60)\times10^{-4}M_{\odot}$ across the same frequency range. We remind the reader that for the extreme phenomenological waveforms considered, $E_{\rm GW}\sim(2\text{–}600)\times10^{-4}M_{\odot}$. This is again consistent with our previous results, as we find that all waveforms are detectable for CCSNe in M31 with the HLV 2019 detector network, but only the more extreme cases are detectable out to M82.

VII. DISCUSSION

The next galactic CCSN will be of great importance to the scientific community, allowing observations of unprecedented accuracy via EM, GW, and neutrino messengers. Using GW waveform predictions for core collapse from state-of-the-art numerical simulations, and phenomenological waveform models for speculative extreme GW emission scenarios, we make the first comprehensive statements on detection prospects for GWs from CCSNe in the Advanced detector era.

Given a known sky location, we outline a search procedure for GW bursts using X-Pipeline, a coherent network analysis pipeline that searches for excess power in time-frequency space, over some astrophysically motivated time period (or on-source window). The GW detector data is non-Gaussian, nonstationary, and often contains loud noise transients. For this reason, it is beneficial to minimize the on-source window to reduce the probability of glitchiness or extreme Gaussian fluctuations being present in the detector data.

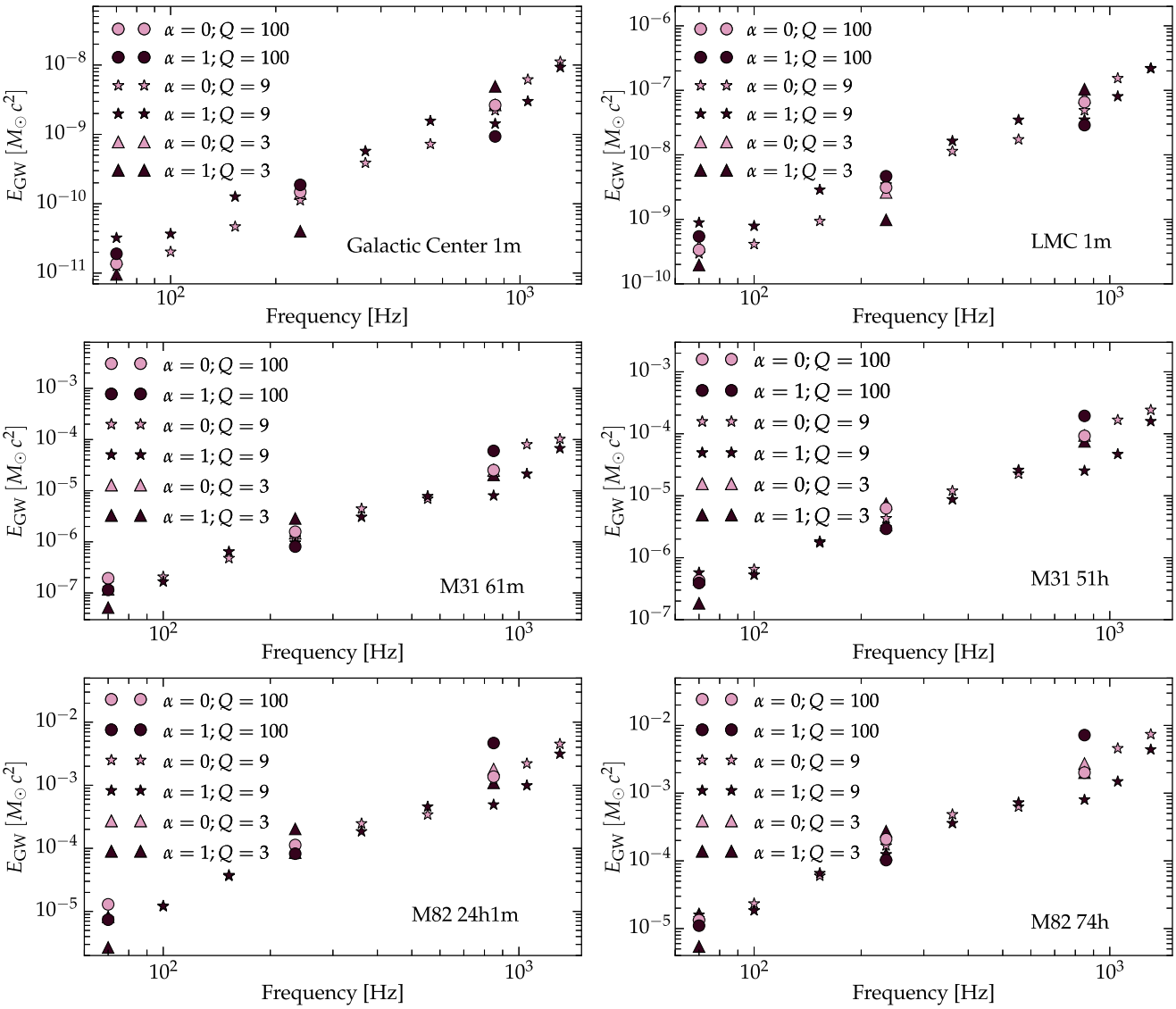

FIG. 8. The energy emitted in GW, $E_{\rm GW}^{50\%}$, required to attain the root-sum-squared strain at 50% detection efficiency, $h_{\rm rss}^{50\%}$, for the sine-Gaussian bursts considered in this study, in the context of the HLV 2019 detector network. The top row is for sources directed toward the Galactic center (left) and the Large Magellanic Cloud (right), for both of which a 1-minute on-source window is used. The middle row is for sources in M31, considering 61-minute and 51-hour on-source windows (left and right plots, respectively). The bottom row is for sources in M82, considering on-source windows of 24 hours and 1 minute, and 74 hours (left and right plots, respectively). Distances of 10 kpc, 50 kpc, 0.77 kpc, and 3.52 Mpc are used to compute $E_{\rm GW}^{50\%}$ for sources in the galaxy, Large Magellanic Cloud, M31, and M82, respectively.

For CCSNe within ∼100 kpc, the coincident neutrino signal will be detected, allowing the time of core collapse to be determined to within a few tens of milliseconds. Using an conservative asymmetric on-source window of $[-10, +50]$ seconds around the start time of the neutrino signal, we consider hypothetical CCSNe in the direction of the Galactic center and the LMC. We find that neutrino-driven CCSN explosions, believed to account for ∼99% for CCSNe, will be detectable within 2.4 kpc, 3.5 kpc, and 5.5 kpc in 2015, 2017, and 2019, respectively. Rapidly rotating CCSNe, however, will be detectable throughout the galaxy from 2017, and the most rapidly rotating model considered will be detectable out to the LMC in 2019. Rapidly rotating CCSNe with nonaxisymmetric rotational instabilities will be detectable out to the LMC and beyond from 2015.

More distant CCSNe will not have coincident neutrino observations, and so the on-source window must be derived using EM observations. Using recent studies of light curves for type Ibc and type II CCSNe (see, e.g. [135–137]), we assume that, if the time of shock breakout $t_{\rm SB}$ is observed, the time of core collapse can be localized to between 1 minute and 50 hours. Unfortunately, shock breakout is rarely observed, and an observation cadence time delay,

$t_{\rm obs}$, between the last pre-CCSN and first post-CCSN images is introduced. Given this, we construct an on-source window of $[-t_{\rm SB}, t_{\rm obs}]$ about the time of the last pre-CCSN image. Frequently observed galaxies, such as those for which the CCSN rate is high, are likely to have CCSNe detected within one day of shock break-out. As such, we consider two observational scenarios where $t_{\rm obs} = 1$ hour and 24 hours for hypothetical CCSNe in M31 and M82, respectively. In the context of EM observations of type Ibc CCSNe, we use on-source windows of 61 minutes and 24 hour 1 minute for CCSNe in M31 and M82, respectively. Correspondingly for type II CCSNe, we use on-source windows of 51 hours and 74 hours for CCSNe in M31 and M82, respectively. We find that most of the extreme GW emission models considered are observable out to M31 with the `HL 2015` detector network when using a 61-minute on-source window, while all models are observable when using the 51 hour on-source window in 2019. Only the most extreme emission models considered are observable out to M82 with the `HL 2015` detector network, but approximately half of the models considered will be detectable out to M82 and beyond in 2019. This allows us to either detect events associated with or exclude such extreme emission models for CCSNe in M31 and M82 with the `HLV 2019` detector network.

In anticipation of unexpected GW emission from CCSNe, we additionally consider sine-Gaussian bursts across the relevant frequency range for all observational scenarios studied. We find that the sensitivity of our search method is comparable, if not slightly improved, to that found for the realistic waveform models considered. This is to be expected as `X-Pipeline`, and other clustering-based burst search algorithms, are most sensitive to short bursts of GW energy localized in frequency space. It should be noted, however, that such simple waveform morphologies are more susceptible to being confused for noise transients. As such, a more complicated waveform morphology, as found for realistic GW predictions for CCSNe, can actually improve detectability [178].

Detection prospects for GWs from CCSNe can be improved by refining light curve models for CCSNe, and increasing observation cadence, so as to reduce the on-source window as derived from EM observations as much as possible. Improvement of stationarity and glitchiness of detector data, in addition to increasing the detector duty cycle, will improve detectability of GWs from CCSNe. Further to this, more second-generation GW detectors such as KAGRA and LIGO India will improve the overall sensitivity of the global GW detector network and could potentially allow for neutrino-driven CCSN explosions to be observable throughout the Galaxy.

ACKNOWLEDGMENTS

The authors thank Alan Weinstein, Peter Kalmus, Lucia Santamaria, Viktoriya Giryanskaya, Valeriu Predoi, Scott Coughlin, James Clark, Michał Wąs, Marek Szczepanczyk, Beverly Berger, and Jade Powell for many fruitful discussions that have benefitted this paper greatly. We thank the CCSN simulation community for making their gravitational waveform predictions available for this study. LIGO was constructed by the California Institute of Technology and Massachusetts Institute of Technology with funding from the National Science Foundation, and operates under cooperative agreement No. PHY-0757058. Advanced LIGO was built under Award No. PHY-0823459. C. D. O. is partially supported by National Science Foundation Grants No. PHY-1404569 and No. CAREER PHY-1151197 and by the Sherman Fairchild Foundation. This paper carries LIGO Document No. LIGO-P1400233.

[1] C. D. Ott, Classical Quantum Gravity **26**, 063001 (2009).
[2] K. Kotake, C.R. Phys. **14**, 318 (2013).
[3] K. Hirata, T. Kajita, M. Koshiba, M. Nakahata, Y. Oyama, N. Sato, A. Suzuki, M. Takita, Y. Totsuka, T. Kifune *et al.*, Phys. Rev. Lett. **58**, 1490 (1987).
[4] R. M. Bionta, G. Blewitt, C. B. Bratton, D. Casper, A. Ciocio, R. Claus, B. Cortez, M. Crouch, S. T. Dye, S. Errede *et al.*, Phys. Rev. Lett. **58**, 1494 (1987).
[5] N. Panagia, in *New Views of the Magellanic Clouds*, edited by Y.-H. Chu, N. Suntzeff, J. Hesser, and D. Bohlender, Vol. 190 of IAU Symposium, (Astronomical Society of the Pacific, San Francisco, 1999), p. 549.
[6] C. W. Misner, K. S. Thorne, and J. A. Wheeler, *Gravitation* (W. H. Freeman and Company, San Francisco, 1973).
[7] K. S. Thorne, in *300 Years of Gravitation*, edited by S. W. Hawking and W. Israel (Cambridge University Press, Cambridge, England, 1987).
[8] É. É. Flanagan and S. A. Hughes, New J. Phys. **7**, 204 (2005).
[9] J. D. E. Creighton and W. G. Anderson, *Gravitational-Wave Physics and Astronomy* (Wiley-VCH, Weinheim, Germany, 2011).
[10] C. D. Ott, Classical Quantum Gravity **26**, 204015 (2009).
[11] J. Logue, C. D. Ott, I. S. Heng, P. Kalmus, and J. H. C. Scargill, Phys. Rev. D **86**, 044023 (2012).
[12] J. W. Murphy, C. D. Ott, and A. Burrows, Astrophys. J. **707**, 1173 (2009).

[13] B. Müller, H.-T. Janka, and A. Marek, Astrophys. J. **766**, 43 (2013).
[14] K. N. Yakunin, P. Marronetti, A. Mezzacappa, S. W. Bruenn, C.-T. Lee, M. A. Chertkow, W. R. Hix, J. M. Blondin, E. J. Lentz, O. E. Bronson Messer *et al.*, Classical Quantum Gravity **27**, 194005 (2010).
[15] K. N. Yakunin, A. Mezzacappa, P. Marronetti, S. Yoshida, S. W. Bruenn, W. R. Hix, E. J. Lentz, O. E. B. Messer, J. A. Harris, E. Endeve *et al.*, Phys. Rev. D **92**, 084040 (2015).
[16] T. Z. Summerscales, A. Burrows, L. S. Finn, and C. D. Ott, Astrophys. J. **678**, 1142 (2008).
[17] H. Dimmelmeier, C. D. Ott, A. Marek, and H.-T. Janka, Phys. Rev. D **78**, 064056 (2008).
[18] K. Hayama, S. Desai, K. Kotake, S. D. Mohanty, M. Rakhmanov, T. Summerscales, and S. Yoshida, Classical Quantum Gravity **25**, 184022 (2008).
[19] E. B. Abdikamalov, C. D. Ott, L. Rezzolla, L. Dessart, H. Dimmelmeier, A. Marek, and H. T. Janka, Phys. Rev. D **81**, 044012 (2010).
[20] C. Röver, M. A. Bizouard, N. Christensen, H. Dimmelmeier, I. S. Heng, and R. Meyer, Phys. Rev. D **80**, 102004 (2009).
[21] A. Marek, H.-T. Janka, and E. Müller, Astron. Astrophys. **496**, 475 (2009).
[22] L. Wang and J. C. Wheeler, Annu. Rev. Astron. Astrophys. **46**, 433 (2008).
[23] R. Chornock, A. V. Filippenko, W. Li, G. H. Marion, R. J. Foley, M. Modjaz, M. Rafelski, G. D. Becker, W. H. de Vries, P. Garnavich *et al.*, Astrophys. J. **739**, 41 (2011).
[24] N. Smith, S. B. Cenko, N. Butler, J. S. Bloom, M. M. Kasliwal, A. Horesh, S. R. Kulkarni, N. M. Law, P. E. Nugent, E. O. Ofek *et al.*, Mon. Not. R. Astron. Soc. **420**, 1135 (2012).
[25] B. Sinnott, D. L. Welch, A. Rest, P. G. Sutherland, and M. Bergmann, Astrophys. J. **767**, 45 (2013).
[26] S. E. Boggs, F. A. Harrison, H. Miyasaka, B. W. Grefenstette, A. Zoglauer, C. L. Fryer, S. P. Reynolds, D. M. Alexander, H. An, D. Barret *et al.*, Science **348**, 670 (2015).
[27] K. Kotake, K. Sumiyoshi, S. Yamada, T. Takiwaki, T. Kuroda, Y. Suwa, and H. Nagakura, Prog. Theor. Exp. Phys. **2012**, 1A301 (2012).
[28] H.-T. Janka, Annu. Rev. Nucl. Part. Sci. **62**, 407 (2012).
[29] C. D. Ott, E. Abdikamalov, P. Mösta, R. Haas, S. Drasco, E. P. O'Connor, C. Reisswig, C. A. Meakin, and E. Schnetter, Astrophys. J. **768**, 115 (2013).
[30] J. C. Dolence, A. Burrows, J. W. Murphy, and J. Nordhaus, Astrophys. J. **765**, 110 (2013).
[31] F. Hanke, B. Müller, A. Wongwathanarat, A. Marek, and H.-T. Janka, Astrophys. J. **770**, 66 (2013).
[32] P. Mösta, S. Richers, C. D. Ott, R. Haas, A. L. Piro, K. Boydstun, E. Abdikamalov, C. Reisswig, and E. Schnetter, Astrophys. J. Lett. **785**, L29 (2014).
[33] S. M. Couch and E. P. O'Connor, Astrophys. J. **785**, 123 (2014).
[34] E. J. Lentz, S. W. Bruenn, W. R. Hix, A. Mezzacappa, O. E. B. Messer, E. Endeve, J. M. Blondin, J. A. Harris, P. Marronetti, and K. N. Yakunin, Astrophys. J. Lett. **807**, L31 (2015).
[35] T. Melson, H.-T. Janka, and A. Marek, Astrophys. J. Lett. **801**, L24 (2015).
[36] J. M. Blondin, A. Mezzacappa, and C. DeMarino, Astrophys. J. **584**, 971 (2003).
[37] E. Müller, H.-T. Janka, and A. Wongwathanarat, Astron. Astrophys. **537**, A63 (2012).
[38] T. Kuroda, T. Takiwaki, and K. Kotake, Phys. Rev. D **89**, 044011 (2014).
[39] C. D. Ott, E. Abdikamalov, E. O'Connor, C. Reisswig, R. Haas, P. Kalmus, S. Drasco, A. Burrows, and E. Schnetter, Phys. Rev. D **86**, 024026 (2012).
[40] C. D. Ott, C. Reisswig, E. Schnetter, E. O'Connor, U. Sperhake, F. Löffler, P. Diener, E. Abdikamalov, I. Hawke, and A. Burrows, Phys. Rev. Lett. **106**, 161103 (2011).
[41] C. L. Fryer, D. E. Holz, and S. A. Hughes, Astrophys. J. **565**, 430 (2002).
[42] M. H. P. M. van Putten, A. Levinson, H. K. Lee, T. Regimbau, M. Punturo, and G. M. Harry, Phys. Rev. D **69**, 044007 (2004).
[43] A. L. Piro and E. Pfahl, Astrophys. J. **658**, 1173 (2007).
[44] A. Corsi and P. Mészáros, Astrophys. J. **702**, 1171 (2009).
[45] J. Weber, Phys. Rev. Lett. **117**, 306 (1960).
[46] P. Aufmuth and K. Danzmann, New J. Phys. **7**, 202 (2005).
[47] P. Astone, M. Bassan, E. Coccia, S. D'Antonio, V. Fafone, G. Giordano, A. Marini, Y. Minenkov, I. Modena, A. Moleti *et al.*, Phys. Rev. D **87**, 082002 (2013).
[48] A. Vinante (for the AURIGA Collaboration), Classical Quantum Gravity **23**, S103 (2006).
[49] O. D. Aguiar *et al.* (Schenberg Collaboration), J. Phys. Conf. Ser. **363**, 012003 (2012).
[50] B. P. Abbott *et al.* (LIGO Scientific Collaboration), Rep. Prog. Phys. **72**, 076901 (2009).
[51] T. Accadia *et al.* (Virgo Collaboration), J. Instrum. **7**, P03012 (2012).
[52] M. Ando *et al.*, Phys. Rev. Lett. **86**, 3950 (2001).
[53] H. Grote and the LIGO Scientific Collaboration, Classical Quantum Gravity **27**, 084003 (2010).
[54] G. M. Harry (for the LIGO Scientific Collaboration), Classical Quantum Gravity **27**, 084006 (2010).
[55] B. Willke *et al.*, Classical Quantum Gravity **23**, S207 (2006).
[56] F. Acernese *et al.* (VIRGO), Classical Quantum Gravity **32**, 024001 (2015).
[57] K. Somiya (for the KAGRA collaboration), Classical Quantum Gravity **29**, 124007 (2012).
[58] B. Iyer *et al.* (IndIGO and LIGO Scientific Collaboration), Tech. Rep. No. LIGO-M1100296-v2, https://dcc.ligo.org/LIGO-M1100296/public.
[59] J. Abadie *et al.* (LIGO Scientific Collaboration and Virgo Collaboration), Phys. Rev. D **85**, 122007 (2012).
[60] J. Abadie, B. P. Abbott, R. Abbott, T. Accadia, F. Acernese, R. Adhikari, P. Ajith, B. Allen, G. Allen, E. Amador Ceron *et al.*, Phys. Rev. D **81**, 102001 (2010).
[61] J. Abadie *et al.* (LIGO Scientific Collaboration and Virgo Collaboration), Astrophys. J. **760**, 12 (2012).
[62] J. Abadie *et al.* (LIGO Scientific Collaboration), Astrophys. J. **755**, 2 (2012).
[63] J. Abadie *et al.* (LIGO Scientific Collaboration), Astrophys. J. Lett. **734**, L35 (2011).

[64] M. Was, P. J. Sutton, G. Jones, and I. Leonor, Phys. Rev. D **86**, 022003 (2012).
[65] N. Arnaud, F. Cavalier, M. Davier, and P. Hello, Phys. Rev. D **59**, 082002 (1999).
[66] T. Zwerger and E. Müller, Astron. Astrophys. **320**, 209 (1997).
[67] M. Ando, T. Akutsu, T. Akutsu, K. Arai, Y. Aso, M. Fukushima, K. Hayama, N. Kanda, K. Kondo, N. Mio *et al.*, Classical Quantum Gravity **22**, S1283 (2005).
[68] W. G. Anderson and R. Balasubramanian, Phys. Rev. D **60**, 102001 (1999).
[69] W. G. Anderson, P. R. Brady, J. D. E. Creighton, and É. É. Flanagan, Phys. Rev. D **63**, 042003 (2001).
[70] A. Viceré, Phys. Rev. D **66**, 062002 (2002).
[71] J. Sylvestre, Phys. Rev. D **68**, 102005 (2003).
[72] H. Dimmelmeier, J. A. Font, and E. Müller, Astron. Astrophys. **393**, 523 (2002).
[73] K. Hayama, T. Kuroda, K. Kotake, and T. Takiwaki, arXiv:1501.00966 (2015).
[74] K. Kotake, W. Iwakami, N. Ohnishi, and S. Yamada, Astrophys. J. Lett. **697**, L133 (2009).
[75] T. Takiwaki and K. Kotake, Astrophys. J. **743**, 30 (2011).
[76] K. Kotake, W. Iwakami-Nakano, and N. Ohnishi, Astrophys. J. **736**, 124 (2011).
[77] K. Hayama, S. D. Mohanty, M. Rakhmanov, and S. Desai, Classical Quantum Gravity **24**, S681 (2007).
[78] P. J. Sutton, G. Jones, S. Chatterji, P. Kalmus, I. Leonor, S. Poprocki, J. Rollins, A. Searle, L. Stein, M. Tinto *et al.*, New J. Phys. **12**, 053034 (2010).
[79] J. F. Beacom and P. Vogel, Phys. Rev. D **60**, 033007 (1999).
[80] G. Pagliaroli, F. Vissani, E. Coccia, and W. Fulgione, Phys. Rev. Lett. **103**, 031102 (2009).
[81] T. Mühlbeier, H. Nunokawa, and R. Z. Funchal, Phys. Rev. D **88**, 085010 (2013).
[82] S. van den Bergh and G. A. Tammann, Annu. Rev. Astron. Astrophys. **29**, 363 (1991).
[83] E. Cappellaro, M. Turatto, S. Benetti, D. Y. Tsvetkov, O. S. Bartunov, and I. N. Makarova, Astron. Astrophys. **273**, 383 (1993).
[84] G. A. Tammann, W. Loeffler, and A. Schroeder, Astrophys. J. Suppl. Ser. **92**, 487 (1994).
[85] W. Li, R. Chornock, J. Leaman, A. V. Filippenko, D. Poznanski, X. Wang, M. Ganeshalingam, and F. Mannucci, Mon. Not. R. Astron. Soc. **412**, 1473 (2011).
[86] R. Diehl, H. Halloin, K. Kretschmer, G. G. Lichti, V. Schönfelder, A. W. Strong, A. von Kienlin, W. Wang, P. Jean, J. Knödlseder *et al.*, Nature (London) **439**, 45 (2006).
[87] S. M. Adams, C. S. Kochanek, J. F. Beacom, M. R. Vagins, and K. Z. Stanek, Astrophys. J. **778**, 164 (2013).
[88] D. Maoz and C. Badenes, Mon. Not. R. Astron. Soc. **407**, 1314 (2010).
[89] F. X. Timmes and S. E. Woosley, Astrophys. J. Lett. **481**, L81 (1997).
[90] H. A. Thronson, Jr., D. A. Hunter, S. Casey, and D. A. Harper, Astrophys. J. **355**, 94 (1990).
[91] K. Gill, M. Zanolin, M. Branchesi, and M. Szczepanczyk (to be published).
[92] S. Ando, J. F. Beacom, and H. Yüksel, Phys. Rev. Lett. **95**, 171101 (2005).
[93] M. D. Kistler, W. C. Haxton, and H. Yüksel, Astrophys. J. **778**, 81 (2013).
[94] M. D. Kistler, H. Yüksel, S. Ando, J. F. Beacom, and Y. Suzuki, Phys. Rev. D **83**, 123008 (2011).
[95] M. T. Botticella, S. J. Smartt, R. C. Kennicutt, E. Cappellaro, M. Sereno, and J. C. Lee, Astron. Astrophys. **537**, A132 (2012).
[96] S. Mattila, T. Dahlen, A. Efstathiou, E. Kankare, J. Melinder, A. Alonso-Herrero, M. Á. Pérez-Torres, S. Ryder, P. Väisänen, and G. Östlin, Astrophys. J. **756**, 111 (2012).
[97] B. P. Abbott, R. Abbott, R. Adhikari, P. Ajith, B. Allen, G. Allen, R. S. Amin, S. B. Anderson, W. G. Anderson, M. A. Arain *et al.*, Phys. Rev. D **80**, 102001 (2009).
[98] J. Abadie, B. P. Abbott, R. Abbott, M. Abernathy, C. Adams, R. Adhikari, P. Ajith, B. Allen, G. Allen, E. Amador Ceron *et al.*, Nucl. Instrum. Methods Phys. Res., Sect. A **624**, 223 (2010).
[99] R. X. Adhikari, Rev. Mod. Phys. **86**, 121 (2014).
[100] J. Aasi, J. Abadie, B. P. Abbott, R. Abbott, T. Abbott, M. R. Abernathy, T. Accadia, F. Acernese, C. Adams, T. Adams *et al.*, Classical Quantum Gravity **32**, 115012 (2015).
[101] J. Aasi, J. Abadie, B. P. Abbott, R. Abbott, T. D. Abbott, M. Abernathy, T. Accadia, F. Acernese, C. Adams, T. Adams *et al.*, Classical Quantum Gravity **29**, 155002 (2012).
[102] L. Blackburn, L. Cadonati, S. Caride, S. Caudill, S. Chatterji, N. Christensen, J. Dalrymple, S. Desai, A. Di Credico, G. Ely *et al.*, Classical Quantum Gravity **25**, 184004 (2008).
[103] T. B. Littenberg and N. J. Cornish, Phys. Rev. D **82**, 103007 (2010).
[104] J. Powell, D. Trifirò, E. Cuoco, I. S. Heng, and M. Cavaglià, Classical Quantum Gravity **32**, 215012 (2015).
[105] R. Biswas, L. Blackburn, J. Cao, R. Essick, K. A. Hodge, E. Katsavounidis, K. Kim, Y.-M. Kim, E.-O. Le Bigot, C.-H. Lee *et al.*, Phys. Rev. D **88**, 062003 (2013).
[106] L. A. Wainstein and V. D. Zubakov, *Extraction of Signals from Noise* (Prentice-Hall, Englewood Cliffs, NJ, 1962).
[107] Goddard Space Flight Center, Lambda Tools Coordinate Conversions, http://lambda.gsfc.nasa.gov/toolbox/tb_coordconv.cfm.
[108] J. R. Thorstensen, R. A. Fesen, and S. van den Bergh, Astron. J. **122**, 297 (2001).
[109] R. C. Kennicutt, Jr. and P. W. Hodge, Astrophys. J. **306**, 130 (1986).
[110] G. de Vaucouleurs, A. de Vaucouleurs, and H. G. Corwin, *Second Reference Catalogue of Bright Galaxies* (University of Texas Press, Austin, 1976).
[111] B. P. Schmidt, R. P. Kirshner, and R. G. Eastman, Astrophys. J. **395**, 366 (1992).
[112] G. Pietrzyński, D. Graczyk, W. Gieren, I. B. Thompson, B. Pilecki, A. Udalski, I. Soszyński, S. Kozłowski, P. Konorski, K. Suchomska *et al.*, Nature (London) **495**, 76 (2013).
[113] I. N. Evans, F. A. Primini, K. J. Glotfelty, C. S. Anderson, N. R. Bonaventura, J. C. Chen, J. E. Davis, S. M. Doe, J. D. Evans, G. Fabbiano *et al.*, Astrophys. J. Suppl. Ser. **189**, 37 (2010).

[114] I. D. Karachentsev, V. E. Karachentseva, W. K. Huchtmeier, and D. I. Makarov, Astron. J. **127**, 2031 (2004).
[115] B. Arbutina, D. Urošević, and B. Vukotić, in *IAU Symposium*, Vol. 237, edited by B. G. Elmegreen and J. Palous (IAU, San Francisco, 2007), p. 391.
[116] N. Jackson, R. A. Battye, I. W. A. Browne, S. Joshi, T. W. B. Muxlow, and P. N. Wilkinson, Mon. Not. R. Astron. Soc. **376**, 371 (2007).
[117] B. A. Jacobs, L. Rizzi, R. B. Tully, E. J. Shaya, D. I. Makarov, and L. Makarova, Astron. J. **138**, 332 (2009).
[118] S. Mattila and W. P. S. Meikle, Mon. Not. R. Astron. Soc. **324**, 325 (2001).
[119] L. Colina and D. Perez-Olea, Mon. Not. R. Astron. Soc. **259**, 709 (1992).
[120] A. Brunthaler, I. Martí-Vidal, K. M. Menten, M. J. Reid, C. Henkel, G. C. Bower, H. Falcke, H. Feng, P. Kaaret, N. R. Butler *et al.*, Astron. Astrophys. **516**, A27 (2010).
[121] P. Antonioli, R. Tresch Fienberg, R. Fleurot, Y. Fukuda, W. Fulgione, A. Habig, J. Heise, A. B. McDonald, C. Mills, T. Namba *et al.*, New J. Phys. **6**, 114 (2004).
[122] M. Aglietta, B. Alpat, E. D. Alyea, P. Antonioli, G. Anzivino, G. Badino, Y. Ban, G. Bari, M. Basile, A. Benelli *et al.*, Il Nuovo Cimento B - Società Italiana di Fisica **105**, 1793 (1992).
[123] M. Ikeda, A. Takeda, Y. Fukuda, M. R. Vagins, K. Abe, T. Iida, K. Ishihara, J. Kameda, Y. Koshio, A. Minamino *et al.*, Astrophys. J. **669**, 519 (2007).
[124] N. Y. Agafonova, M. Aglietta, P. Antonioli, G. Bari, A. Bonardi, V. V. Boyarkin, G. Bruno, W. Fulgione, P. Galeotti, M. Garbini *et al.*, Astropart. Phys. **28**, 516 (2008).
[125] G. Alimonti, C. Arpesella, H. Back, M. Balata, D. Bartolomei, A. de Bellefon, G. Bellini, J. Benziger, A. Bevilacqua, D. Bondi *et al.*, Nucl. Instrum. Methods Phys. Res., Sect. A **600**, 568 (2009).
[126] K. Scholberg, Annu. Rev. Nucl. Part. Sci. **62**, 81 (2012).
[127] R. Abbasi, Y. Abdou, T. Abu-Zayyad, M. Ackermann, J. Adams, J. A. Aguilar, M. Ahlers, M. M. Allen, D. Altmann, K. Andeen *et al.*, Astron. Astrophys. **535**, A109 (2011).
[128] A. Suzuki, Nucl. Phys. B, Proc. Suppl. **77**, 171 (1999).
[129] K. Asakura, A. Gando, Y. Gando, T. Hachiya, S. Hayashida, H. Ikeda, K. Inoue, K. Ishidoshiro, T. Ishikawa, S. Ishio *et al.*, arXiv:1506.01175 (2015).
[130] T. Fischer, S. C. Whitehouse, A. Mezzacappa, F.-K. Thielemann, and M. Liebendörfer, Astron. Astrophys. **517**, A80 (2010).
[131] A. Mirizzi, I. Tamborra, H.-T. Janka, N. Saviano, K. Scholberg, R. Bollig, L. Hüdepohl, and S. Chakraborty, arXiv:1508.00785 (2015).
[132] J. Wallace, A. Burrows, and J. C. Dolence, arXiv: 1510.01338 (2015).
[133] A. V. Filippenko, Annu. Rev. Astron. Astrophys. **35**, 309 (1997).
[134] S. J. Smartt, Annu. Rev. Astron. Astrophys. **47**, 63 (2009).
[135] L.-X. Li, Mon. Not. R. Astron. Soc. **375**, 240 (2007).
[136] M. C. Bersten, O. Benvenuto, and M. Hamuy, Astrophys. J. **729**, 61 (2011).
[137] V. Morozova, A. L. Piro, M. Renzo, C. D. Ott, D. Clausen, S. M. Couch, J. Ellis, and L. F. Roberts, Astrophys. J. **814**, 63 (2015).
[138] LIGO Scientific Collaboration, Virgo Collaboration, J. Aasi, J. Abadie, B. P. Abbott, R. Abbott, T. D. Abbott, M. Abernathy, T. Accadia, F. Acernese *et al.*, arXiv: 1304.0670 (2013).
[139] C. D. Ott, H. Dimmelmeier, A. Marek, H.-T. Janka, I. Hawke, B. Zink, and E. Schnetter, Phys. Rev. Lett. **98**, 261101 (2007).
[140] S. Scheidegger, R. Käppeli, S. C. Whitehouse, T. Fischer, and M. Liebendörfer, Astron. Astrophys. **514**, A51 (2010).
[141] C. Fryer and K. C. B. New, Living Rev. Relativity **14**, 1 (2011).
[142] C. Reisswig, C. D. Ott, U. Sperhake, and E. Schnetter, Phys. Rev. D **83**, 064008 (2011).
[143] S. Scheidegger, S. C. Whitehouse, R. Käppeli, and M. Liebendörfer, Classical Quantum Gravity **27**, 114101 (2010).
[144] C. D. Ott (LIGO Scientific Collaboration), Tech. Rep. No. LIGO-T1000553-v2, https://dcc.ligo.org/LIGO-T1000553/public.
[145] P. Ajith, M. Boyle, D. A. Brown, S. Fairhurst, M. Hannam, I. Hinder, S. Husa, B. Krishnan, R. A. Mercer, F. Ohme *et al.*, arXiv:0709.0093v3 (2007).
[146] A. Burrows, J. C. Dolence, and J. W. Murphy, Astrophys. J. **759**, 5 (2012).
[147] B. Müller, H.-T. Janka, and A. Heger, Astrophys. J. **761**, 72 (2012).
[148] S. M. Couch and C. D. Ott, Astrophys. J. **799**, 5 (2015).
[149] J. Fuller, H. Klion, E. Abdikamalov, and C. D. Ott, Mon. Not. R. Astron. Soc. **450**, 414 (2015).
[150] I. S. Heng, Classical Quantum Gravity **26**, 105005 (2009).
[151] E. Abdikamalov, S. Gossan, A. M. DeMaio, and C. D. Ott, Phys. Rev. D **90**, 044001 (2014).
[152] W. J. Engels, R. Frey, and C. D. Ott, Phys. Rev. D **90**, 124026 (2014).
[153] J. M. Lattimer and F. D. Swesty, Nucl. Phys. **A535**, 331 (1991).
[154] C. D. Ott, S. Ou, J. E. Tohline, and A. Burrows, Astrophys. J. **625**, L119 (2005).
[155] L. Baiotti, R. DePietri, G. M. Manca, and L. Rezzolla, Phys. Rev. D **75**, 044023 (2007).
[156] D. Lai, in *AIP Conf. Proc. 575: Astrophysical Sources for Ground-Based Gravitational Wave Detectors*, edited by J. M. Centrella (AIP, London, 2001), p. 246.
[157] C. D. Ott, A. Burrows, T. A. Thompson, E. Livne, and R. Walder, Astrophys. J. Suppl. Ser. **164**, 130 (2006).
[158] E. Balbinski, Mon. Not. R. Astron. Soc. **216**, 897 (1985).
[159] A. L. Watts, N. Andersson, and D. I. Jones, Astrophys. J. Lett. **618**, L37 (2005).
[160] H.-T. Janka, K. Langanke, A. Marek, G. Martínez-Pinedo, and B. Müller, Phys. Rep. **442**, 38 (2007).
[161] E. O'Connor and C. D. Ott, Astrophys. J. **730**, 70 (2011).
[162] S. E. Woosley and J. S. Bloom, Annu. Rev. Astron. Astrophys. **44**, 507 (2006).
[163] R. Perna, P. J. Armitage, and B. Zhang, Astrophys. J. Lett. **636**, L29 (2006).
[164] L. Santamaria and C. D. Ott (LIGO Scientific Collaboration), Tech. Rep. No. LIGO-T1100093-v2, https://dcc.ligo.org/LIGO-T1100093/public.
[165] J. Abadie, B. P. Abbott, R. Abbott, T. D. Abbott, M. Abernathy, T. Accadia, F. Acernese, C. Adams, R.

Adhikari, C. Affeldt *et al.*, Phys. Rev. D **85**, 022001 (2012).
[166] M. Was, Ph.D. thesis, Université Paris Sud—Paris XI, 2011), https://tel.archives-ouvertes.fr/tel-00610302.
[167] S. Klimenko, S. Mohanty, M. Rakhmanov, and G. Mitselmakher, Phys. Rev. D **72**, 122002 (2005).
[168] S. Klimenko, S. Mohanty, M. Rakhmanov, and G. Mitselmakher, J. Phys. Conf. Ser. **32**, 12 (2006).
[169] P. R. Brady, J. D. E. Creighton, and A. G. Wiseman, Classical Quantum Gravity **21**, S1775 (2004).
[170] R. Biswas, P. R. Brady, J. D. E. Creighton, and S. Fairhurst, Classical Quantum Gravity **26**, 175009 (2009).
[171] S. Chatterji, A. Lazzarini, L. Stein, P. J. Sutton, A. Searle, and M. Tinto, Phys. Rev. D **74**, 082005 (2006).
[172] M. Vallisneri, J. Kanner, R. Williams, A. Weinstein, and B. Stephens, J. Phys. Conf. Ser. **610**, 012021 (2015).
[173] K. Cannon, R. Cariou, A. Chapman, M. Crispin-Ortuzar, N. Fotopoulos, M. Frei, C. Hanna, E. Kara, D. Keppel, L. Liao *et al.*, Astrophys. J. **748**, 136 (2012).
[174] S. Privitera, S. R. P. Mohapatra, P. Ajith, K. Cannon, N. Fotopoulos, M. A. Frei, C. Hanna, A. J. Weinstein, and J. T. Whelan, Phys. Rev. D **89**, 024003 (2014).
[175] J. Abadie *et al.* (The LIGO Scientific Collaboration and The Virgo Collaboration), Phys. Rev. D **85**, 122007 (2012).
[176] P. Kalmus, Ph.D. thesis, Columbia University, 2009.
[177] The LIGO Scientific Collaboration, J. Aasi, B. P. Abbott, R. Abbott, T. Abbott, M. R. Abernathy, K. Ackley, C. Adams, T. Adams, P. Addesso *et al.*, Classical Quantum Gravity **32**, 115012 (2015).
[178] J. B. Kanner, T. B. Littenberg, N. Cornish, M. Millhouse, E. Xhakaj, F. Salemi, M. Drago, G. Vedovato, and S. Klimenko (to be published).